PHYSICAL REVIEW B VOLUME 16, NUMBER 1 1 JULY 1977

Static, quasistatic, and quasidynamic Jahn-Teller effect in the EPR spectra of Ag^{2+} in SrO, CaO, and MgO

L. A. Boatner
Ecole Polytechnique Fédérale de Lausanne, Laboratoire de Physique Expérimentale, CH-1007 Lausanne, Switzerland

R. W. Reynolds
General Research Corporation, Huntsville, Alabama 35807

Y. Chen and M. M. Abraham
Solid State Physics Division, Oak Ridge National Laboratory, Oak Ridge, Tennessee 37830*
(Received 24 March 1977)

The EPR spectra observed for Ag^{2+} in the alkaline-earth–oxide host crystals SrO, CaO, and MgO provide an exceptionally clear example of the unusual spectral features associated with the transition from a static to a dynamic Jahn-Teller effect at low temperature. The spectrum observed for Ag^{2+} in SrO exhibits the low-temperature threefold tetragonal symmetry with symmetric line shapes and averaging at higher temperatures (80 to 200 K) which characterize the static Jahn-Teller (JT) effect. A threefold tetragonally symmetric spectrum is also observed for Ag^{2+} in CaO at 1.3 K, but, in this case, the line shapes are not symmetric and resemble those observed for systems exhibiting a dynamic JT effect. Additionally, a complex line shape is observed at 1.3 K for Ag^{2+} in CaO with the orientation $\vec{H} \parallel [111]$. These line-shape effects are due to a value of the ratio of random strain splitting $\bar{\delta}$ to "tunneling" splitting 3Γ which is intermediate to those associated with either the static or dynamic JT effect. The complex line shapes observed at 9 GHz with $\vec{H} \parallel [111]$ have been computed by performing a numerical diagonalization of the matrix of strain and tunneling for the manifold of states consisting of the ground ^2E and first-excited A_2 vibronic singlet levels. From this calculation a value of 1.2 has been determined for the ratio $\bar{\delta}/3\Gamma$. At a frequency of 23 GHz, the line shapes for Ag^{2+} in CaO exhibit additional effects due to the increased Zeeman interaction, and, by performing a simultaneous diagonalization of the strain, tunneling, and Zeeman matrices, it is possible to independently determine values of 4.7 and 3.9 cm^{-1} for $\bar{\delta}$ and 3Γ, respectively. For Ag^{2+} in MgO, the angular variation of the EPR spectrum at 1.3 K resembles the type of variation typical of a dynamic JT system, but with one component shifted and broadened by coupling via random strain to a nearly excited A_2 vibronic singlet level. A value of $\bar{\delta}/3\Gamma = 0.13$ was determined for Ag^{2+} in MgO by fitting the observed angular variation to a computed angular variation derived from a numerical diagonalization of the matrix of strain and tunneling for the ^2E-A_2 manifold. These observed features classify the JT effect as static, quasistatic, and quasidynamic for Ag^{2+} in SrO, CaO, and MgO, respectively.

I. INTRODUCTION

Early EPR investigations of the orbitally degenerate ground states of impurity ions which were incorporated into high-symmetry hosts and which were, accordingly, subject to a configurational instability as a consequence of the Jahn-Teller theorem, resulted in the identification of a number of systems characterized by the limiting case known as the "static" Jahn-Teller effect.[1,2] Somewhat later, for the particular case of ions with ^2E orbital ground states, EPR spectra were observed[3-5] whose features were completely different from those found previously for systems exhibiting the static Jahn-Teller effect. This new type of Jahn-Teller (JT) spectrum was characterized at low temperature by an anisotropy appropriate to an ^2E state in a cubic symmetry crystal field instead of the three magnetically inequivalent, tetragonally symmetric spectra associated with the static Jahn-Teller effect. The extreme differences (relative to the static case) exhibited by the new spectra were attributed to a manifestation of the zero-point motion of the lattice which resulted in a "dynamic" effect at low temperature. Initial interpretations of this low-temperature dynamic effect were based on the "tunneling" model of O'Brien[6] and Bersuker.[7-9] In this model, tunneling occurs between the potential barriers which separate the three tetragonally distorted "static" Jahn-Teller configurations and results in a splitting of the ground state into a ^2E vibronic ground level and excited A_1 and A_2 vibronic singlets. The model of O'Brien[6] and Bersuker[7-9] is only appropriate to those systems in which the Jahn-Teller coupling is strong and the system is close to the static JT limit.

Subsequent to the work of Bersuker and O'Brien, an alternate interpretation of the low-temperature "dynamic" JT spectra was proposed by Ham.[10] This interpretation, which was based partially on the previous work of Longuet-Higgins *et al.*[11,12] and Moffitt *et al.*,[13,14] was appropriate to systems where the JT coupling was weak to moderate in

contrast to the model of Bersuker or O'Brien with its inherent assumption of strong JT coupling. Ham demonstrated that the unusual line shapes observed for the low-temperature dynamic systems resulted from the effects of large random strains present in the host crystal. Additionally, Ham formulated an effective Hamiltonian which included the effects of random strain and which accurately described the features of observed dynamic JT spectra while relating these features to the strength of the vibronic coupling. These theoretical formulations provided the impetus for a whole series[15-19] of ensuing experimental EPR investigations which dealt principally with the d^1-configuration ions Sc^{2+}, Y^{2+}, and La^{2+} in the fluorite-structure alkaline-earth halides. In the course of these investigations, spectroscopic features were observed which required the addition of a quadrupole term to the effective Hamiltonian, and second-order solutions to the Hamiltonian were obtained which properly accounted for the observed angular variations.

Investigations of the d^1-configuration ions, as noted above, resulted in the characterization of a number of excellent examples of systems for which the JT coupling was weak to moderate. This information, together with that available from the earlier studies of systems exhibiting a static JT effect, provided a clear picture of the spectral features of ^2E systems which represented the limiting dynamic and static cases of the JT effect. Since the EPR spectra are fundamentally quite different for these two limiting cases, an important question remained regarding the nature of the spectra in the transition region between a "pure dynamic" and a "pure static" JT effect. An indication of what some of the spectral features might be in an intermediate system was provided by the results of an experiment by Chase[20,21] who employed optically detected resonance techniques in the investigation of an excited ^2E level of Eu^{2+} in CaF_2 and SrF_2. This work showed that when the first-excited vibronic A_1 or A_2 singlet was sufficiently close to the ground ^2E vibronic level, coupling between the ^2E and $A_1(A_2)$ levels would lead to an asymmetric broadening of the spectrum. In conjunction with the experimental work on Eu^{2+}, a three-state vibronic coupling model was developed which described the transition from a dynamic to a static JT effect in the limit of strong vibronic coupling.

Although these theoretical formulations[1,21] provided a basis for the analysis of intermediate JT systems, this work was followed by a period of several years during which there was an absence of published results on systems in which the presence of intermediate JT effects was established. This situation was markedly altered when it was discovered[22] that the EPR spectra of Ag^{2+} in the isomorphic series of alkaline-earth–oxide hosts SrO, CaO, and MgO provided an excellent example of the transition from a static JT effect to an "almost dynamic" effect with two of the systems (i.e., $CaO:Ag^{2+}$ and $MgO:Ag^{2+}$) representing intermediate cases. Subsequently, it was also shown[23] that the $CaO:Cu^{2+}$ and $MgO:Cu^{2+}$ systems investigated by Coffman[4,5] were actually systems which exhibited intermediate JT coupling effects. In conjunction with the experimental work on Ag^{2+} and Cu^{2+} in the oxide hosts noted above, two of us (R.W.R. and L.A.B.) investigated in detail[24] the general implications of the three-state formalism which describes the transition from a dynamic to a static JT effect. As a cumulative result of these efforts, it has now been established that intermediate Jahn-Teller effects for ^2E orbital states are evidenced by the presence of one or more of the following features: (i) an angular variation which is neither characteristic of tetragonal symmetry nor of full cubic symmetry, but is intermediate to both (See Figs. 3 and 4 of Ref. 24 for examples); (ii) a broadening and shifting of spectral components which is selective in regard to the portion of the spectrum that is affected (See Figs. 2 and 9 of Ref. 24); (iii) an unusual structure for the EPR line shapes found for the orientation $\vec{H} \| \langle 111 \rangle$ (See Figs. 6 and 7 of Ref. 24).

Since the EPR spectra observed for Ag^{2+} in SrO, CaO, and MgO exhibit, in one host or another, all of the above characteristics, a complete presentation of the experimental results and the special analysis for this system is desirable. Accordingly, the present article is directed toward three major purposes. First, the results for the Ag^{2+}–alkaline-earth–oxide system, which has been the subject of preliminary reports,[22,25-27] will be presented in detail. Second, a new technique for independently determining the magnitudes of the average strain splitting and the tunneling splitting in intermediate JT systems will be discussed. The ability to make a determination of this type has been developed since the publication of Ref. 22, and it affords a number of interesting possibilities for the study of random strains in the refractory oxides. Finally, the properties of the Ag^{2+} EPR spectra observed at elevated temperatures and the associated high-temperature averaging processes will be examined in some detail for the three cases represented by the EPR spectra of divalent silver in the alkaline-earth–oxide hosts.

II. THEORY

The primary aspects of the theory associated with the transition from a static to a dynamic

Jahn-Teller effect have recently been the subject of a detailed treatment by Reynolds and Boatner.[24] Accordingly, the present discussion will only briefly review those aspects of the theory which are directly pertinent to the interpretation of the EPR spectra observed for Ag^{2+} in SrO, CaO, and MgO and which also provide the background for a necessary extension of the theory as treated in the Appendix.

Divalent silver has an electronic configuration consisting of nine $4d$ electrons with a krypton core. For a d^9-configuration ion in a sixfold-coordinated cubic crystal field, a ^2E electronic state lies lowest, and the first-excited electronic state is a triplet $^2T_2$ level. Coupling between the ground ^2E orbital state and the vibrational modes of the cluster formed by the Ag^{2+} ion and its nearest neighbors via JT linear coupling and warping interactions results in a vibronic energy-level structure characterized by a ^2E vibronic ground state and excited vibronic A_1 and A_2 singlet levels.[1] The signs and magnitudes of the JT linear and warping parameters determine which singlet (i.e., A_1 or A_2) lies lower, and the singlets become accidentally degenerate as the warping terms become negligible. Other vibronic levels are present at higher energies, and a calculation of their relative energies has been made by O'Brien[6] for the case of strong JT coupling. The presence of such excited vibronic states has been confirmed experimentally, and Raman scattering measurements of their energy relative to the ground-vibronic ^2E state have been made by Guha and Chase[28] for the case of Cu^{2+} in CaO. The characteristics of the EPR spectra for nearly all cubic symmetry systems having ^2E orbital ground states can be predicted by considerations employing only the three lowest vibronic levels, the ^2E vibronic ground doublet and the lowest vibronic singlet. (The EPR spectrum of Cu^{2+} in MgO is the major exception to the above.[23]) The observed EPR spectra result from the effects of the random strain, Zeeman, and (if appropriate) hyperfine and quadrupole interactions operating within the three lowest vibronic levels.

The energy difference between the ^2E vibronic ground state and the nearest A_1 or A_2 vibronic singlet is designated as the "tunneling" splitting and is denoted by the symbol 3Γ. Random strains in the host crystal produce a splitting of the ground ^2E vibronic state with an average strain splitting $\bar{\delta}$ which is usually greater than the Zeeman splitting at an EPR frequency of 10 GHz. The ratio $\bar{\delta}/3\Gamma$ then determines whether static, intermediate, or dynamic JT effects are observed. For the large values of $\bar{\delta}/3\Gamma$ which occur as the excited vibronic A_1 or A_2 singlet approaches the ground ^2E level, a static JT effect is observed. On the other hand, when the tunneling splitting is sufficiently large relative to the random strain and Zeeman splittings, the EPR spectrum is characteristic of the isolated, strain-split ^2E vibronic level and a dynamic JT effect is observed. Intermediate JT effects occur when the random strain (or Zeeman) splittings are comparable to the tunneling splitting 3Γ. We have found previously that the various JT effects observed for ^2E systems can be conveniently classified by the use of four general (and slightly overlapping) categories. These are as follows:

(a) For those cases where three tetragonal symmetry spectra are observed and where the line shapes of such spectra have the usual Gaussian or Lorentzian form, the JT effect is denoted as "pure static." In general, this classification corresponds to $\bar{\delta}/3\Gamma > 5$.

(b) When three tetragonally symmetric EPR spectra are observed but are accompanied by the presence of distorted line shapes similar to those found for dynamic systems, the JT effect is termed "quasistatic." This classification is associated with a range of $\bar{\delta}/3\Gamma$ values less than 5.0 and greater than 0.3.

(c) The classification "quasidynamic" is applied to those spectra where the observed angular variation is similar to the angular variation appropriate to an isolated ^2E state and three tetragonally symmetric spectra are not observed. The angular variation for this category is not identical to that found for an isolated ^2E state in that one component of the spectrum is shifted (and broadened) by coupling via strain to the nearest excited vibronic singlet. This category applies to systems where $\bar{\delta}/3\Gamma$ lies in the range $0.1 < \delta/3\Gamma < 0.8$.

(d) When the ^2E vibronic state is separated from the first-excited vibronic singlet A_1 or A_2 by an energy difference which is large in comparison with that associated with perturbations (such as the strain or Zeeman interaction) which could couple the ground and excited states, the JT effect is denoted as "pure dynamic," and a spectrum appropriate only to the isolated strain-split ^2E state is observed. This occurs for values of $\bar{\delta}/3\Gamma$ less than 0.1. The low-temperature EPR spectrum of Sc^{2+} in CaF_2, SrF_2, and BaF_2 has been successfully described by considering only the ^2E vibronic ground state, and the reader is referred to Refs. 15–19 for a detailed description of pure dynamic JT effects.

In treating the limiting case of the static JT effect as well as both categories of intermediate (i.e., quasistatic and quasidynamic) effects, it is convenient to express the perturbing interactions relative to the vibronic states ψ_1, ψ_2, and ψ_3 de-

fined as follows[1]:

$$\Psi_{A1}=(1/\sqrt{3})(\Psi_1+\Psi_2+\Psi_3)\,,$$
$$\Psi_{g\theta}=(1/\sqrt{6})(2\Psi_1-\Psi_2-\Psi_3),\quad \Psi_{g\epsilon}=(1/\sqrt{2})(\Psi_2-\Psi_3),$$

with A_1 lowest or, with A_2 lowest, as

$$\Psi_{A2}=(1/\sqrt{3})(\Psi_1+\Psi_2+\Psi_3),\quad \Psi_{g\theta}=(1/\sqrt{2})(\Psi_3-\Psi_2),$$
$$\Psi_{g\epsilon}=(1/\sqrt{6})(2\Psi_1-\Psi_2-\Psi_3), \tag{1}$$

where $\psi_{g\theta}$ and $\psi_{g\epsilon}$ are the components of the ^2E vibronic ground state having the transformation properties indicated by the respective subscripts. For strong JT coupling with warping (such that the Ham reduction factors[1] are related by $r=-\sqrt{2}\,q$) and with the random strain and tunneling interactions large compared to the Zeeman interaction, the matrices of strain and tunneling expressed relative to the ψ_1,ψ_2,ψ_3 basis are as follows[1]:

$$\begin{array}{c} \\ \Psi_1: \\ \Psi_2: \\ \Psi_3: \end{array}\begin{array}{c} \begin{array}{ccc} \Psi_1 & \Psi_2 & \Psi_3 \end{array} \\ \begin{bmatrix} \Gamma\mp\delta\cos\phi/2q & \Gamma & \Gamma \\ \Gamma & \Gamma\pm\delta(\cos\phi-\sqrt{3}\,\sin\phi)/2q & \Gamma \\ \Gamma & \Gamma & \Gamma\pm\delta(\cos\phi+\sqrt{3}\,\sin\phi)/2q \end{bmatrix}, \end{array} \tag{2}$$

where the upper signs correspond to A_1 lower and the lower signs to A_2 lower. In Eq. (2), δ is given by

$$\delta=2q\,|V_2|\,(e_\theta^2+e_\epsilon^2)^{1/2}, \tag{3}$$

where V_2 is the strain coupling parameter, e_θ and e_ϵ are the components of the tetragonal strain, and $\tan\phi=e_\epsilon/e_\theta$. The EPR spectrum for the conditions noted above can then be computed by a numerical diagonalization of Eq. (2) and the Zeeman interaction treated by first-order perturbation theory using the eigenstates resulting from this diagonalization.

From Eq. (2) it can be seen that for $\delta\gg 3\Gamma$, the eigenvectors are simply ψ_1, ψ_2, and ψ_3. Within each of these three Kramers doublets, the expectation values of the Zeeman interaction are given by the following expressions:

$$\begin{aligned}
\mathcal{H}_{11}&=\Gamma+g_\parallel\mu_B H_z S_z+g_\perp\mu_B(H_xS_x+H_yS_y)\\
&\quad+A_\parallel S_zI_z+A_\perp(S_xI_x+S_yI_y),\\
\mathcal{H}_{22}&=\Gamma+g_\parallel\mu_B H_x S_x+g_\perp\mu_B(H_zS_z+H_yS_y)\\
&\quad+A_\parallel S_xI_x+A_\perp(S_zI_z+S_yI_y),\\
\mathcal{H}_{33}&=\Gamma+g_\parallel\mu_B H_y S_y+g_\perp\mu_B(H_xS_x+H_zS_z)\\
&\quad+A_\parallel S_yI_y+A_\perp(S_xI_x+S_zI_z).
\end{aligned} \tag{4}$$

The relationships between $g_\parallel$, $g_\perp$, $A_\parallel$, and $A_\perp$ and the effective Hamiltonian parameters g_1, qg_2, A_1, qA_2 used to describe the dynamic JT effect[29] are as follows:

$$g_\parallel=g_1\mp 2qg_2,\quad g_\perp=g_1\pm qg_2,$$
$$A_\parallel=A_1\mp 2qA_2,\quad A_\perp=A_1\pm qA_2, \tag{5}$$

where the upper sign is appropriate to having the A_1 vibronic singlet lower and the lower sign to having the A_2 state lower. The relations given by Eq. (4) correspond to an EPR spectrum consisting of the three magnetically equivalent spectra with tetragonal symmetry which characterize the static JT effect.

As discussed previously, intermediate effects are manifested by a selective shift and broadening of the spectral components relative to an otherwise "pure dynamic" or "pure static" EPR spectrum. The relation of the components thus affected to the sign of qg_2 and to which vibronic singlet (A_1 or A_2) lies lower has been discussed in detail in Ref. 24. Once the sign of qg_2 is known, the singlet responsible for the observed intermediate JT effects can be identified using Table I of Ref. 24. For quasidynamic cases, the effective Hamiltonian parameters g_1, qg_2, A_1, and qA_2 can be determined by fitting the angular variation of those spectral components which are not affected by coupling to the vibronic singlet level to Eq. (3) of Ref. 18. The ratio $\bar{\delta}/3\Gamma$ can then be determined by fitting the angular variation of the components which do exhibit the effects of ^2E-$A_{1,2}$ coupling by means of a numerical diagonalization of the matrix given in Eq. (2). For quasistatic systems, the angular variation has, by definition, tetragonal symmetry and in such cases, in order to determine $\bar{\delta}/3\Gamma$, it is necessary to fit the line shapes observed for the orientation of the applied magnetic field corresponding to $\vec{H}\|\langle 111\rangle$ by means of a numerical diagonalization of the matrix in Eq. (2). When the Zeeman interaction is not sufficiently small in comparison with the strain and tunneling interactions, a simultaneous diagonalization of the matrix of strain, tunneling, and Zeeman interactions must be performed. However, by utilizing a relatively low microwave frequency, so that the as-

sumptions inherent in formulating the matrix in Eq. (2) are satisfied, it is possible to accurately determine g_1, qg_2, A_1, qA_2, and $\bar{\delta}/3\Gamma$ as previously noted. Then, by using a significantly higher microwave frequency and performing a numerical diagonalization of the matrix including the larger Zeeman interaction, it is possible to determine the ratio of 3Γ to the Zeeman interaction and hence to evaluate 3Γ. The value of $\bar{\delta}$ can be determined since the ratio $\bar{\delta}/3\Gamma$ is determined from the EPR data obtained at the lower microwave frequency. The details of the formulation which explicitly includes the Zeeman interaction will be treated in the Appendix, where a procedure of the type described above has been used to independently determine $\bar{\delta}$ and 3Γ for Ag^{2+} in CaO from a fit to the line shapes observed for $\vec{H}\|\langle 111\rangle$ at 8.8 and 23.0 GHz.

III. RESULTS

The SrO, CaO, and MgO single crystals employed in this investigation were grown by an arc-fusion technique[30] with the silver dopant added to the starting powder in the form of AgO. For all three types of host crystal, no spectra due to Ag^{2+} could be detected in the "as grown" samples. In each case it was necessary to irradiate the crystals with short-wavelength ultraviolet light for periods ranging from 4 to 48 h in order to observe the Ag^{2+} spectrum. Following a room-temperature uv irradiation, the divalent charge state remained stable for a period of several days with the sample stored at room temperature.

The X-band spectrometer ($\nu \approx 8.8$ GHz) and the K-band spectrometer (23 GHz) both utilized "back diode" detectors in order to realize low-noise performance with the magnetic field modulated at a frequency of 2 kHz. At X band, a TE_{011}-mode cylindrical cavity was used, which provided for sample interchangeability at helium temperatures and for *in situ* orientation of the single crystals. A cylindrical TE_{012}-mode cavity was employed in the measurements made at K band, and this cavity also permitted *in situ* crystal orientation. The ability to perform *in situ* orientations by rotating the sample in a vertical plane (and the magnetic field in the horizontal plane) while observing the first-derivative presentation of the EPR absorption signal on an oscilloscope was essential. In particular, the accuracy with which the orientation must be carried out (better than 0.1°) in order to obtain an accurate line shape with $\vec{H}\|\langle 111\rangle$ makes an external x-ray orientation and sample transfer prohibitively difficult.

A. Ag^{2+} in SrO

The SrO:Ag^{2+} single crystals employed in this investigation were grown from starting material in the form of high-purity strontium carbonate. Following the uv irradiation at room temperature, an EPR examination at X band and 4.2 K resulted in the observation of the Ag^{2+} spectrum as well as an unknown anisotropic spectrum. No other spectra due either to paramagnetic impurity ions or to color centers were observed in the SrO crystals. At 4.2 K, the EPR spectrum of Ag^{2+} in SrO was characterized by the presence of three tetragonally symmetric spectra whose principal symmetry axes lay along the three $\langle 100\rangle$ crystallographic axes of the host. For three axial sites which are symmetry related in this manner, it is possible to observe the resonance spectra for the applied magnetic field $\vec{H}$ perpendicular to the principal symmetry axes at two different orientations of $\vec{H}$ in a $\{110\}$ plane. These orientations are 90° apart and correspond to $\vec{H}\|\langle 100\rangle$, where the applied field is perpendicular to the principal axis of two of the three sites and to $\vec{H}\|\langle 110\rangle$, where the field is perpendicular to the principal axis of one of the three sites. As can be seen from Fig. 3 of Ref. 24, intermediate JT effects near the static limit are manifested in changes in the angular variation such that the magnetic field values for the resonance absorption at the two "perpendicular" orientations

TABLE I. Effective Hamiltonian parameters for Ag^{2+} in SrO, CaO, and MgO.

Static and quasistatic Jahn-Teller effect							
Host	$\frac{\bar{\delta}}{3\Gamma}$	$g_\parallel$	$g_\perp$	$^{107}A_\parallel$ (10^{-4} cm^{-1})	$^{109}A_\parallel$ (10^{-4} cm^{-1})	$^{107}A_\perp$ (10^{-4} cm^{-1})	$^{109}A_\perp$ (10^{-4} cm^{-1})
SrO	•••	2.112±0.001	2.017±0.001	28.79±0.02	33.31±0.002	22.92±0.02	26.61±0.02
CaO	1.2	2.166±0.001	2.031±0.001	29.4±0.4	34.0±0.4	21.0±0.3	24.8±0.3

Dynamic and quasidynamic Jahn-Teller effect					
Host	$\frac{\bar{\delta}}{3\Gamma}$	g_1	qg_2	A_1 (10^{-4} cm^{-1})	qA_2 (10^{-4} cm^{-1})
MgO	0.13	2.0998±0.0007	+0.0563±0.0007	25.8±0.2	5.4±0.8

noted above are not equal. Accordingly, for Ag^{2+} in SrO, particular attention was given to measurements of the values for $g_\perp$ at the orientations $\vec{H}\|[100]$ and $\vec{H}\|[110]$ in the $(1\bar{1}0)$ plane. The magnetic field positions (or $g_\perp$ values) were found to be equal to within the experimental error of $\frac{1}{10}$ of the linewidth or about 0.1 G. [An excellent example of a situation where the magnetic field positions are only slightly different for the perpendicular orientations with $\vec{H}\|[100]$ and $\vec{H}\|[110]$ is given by the case of Cu^{2+} in CaO (see Fig. 5 of Ref. 23).] The effective Hamiltonian parameters which describe the low-temperature tetragonal spectra for Ag^{2+} in SrO are given in Table I. These parameters were determined using a computer technique based on an exact calculation of the eigenvectors, eigenvalues, and transition probabilities and an ensuing least-squares fit in which all of the parameters were varied to give transition energies equivalent to the microwave energy. For Ag^{2+} in SrO, the observed linewidths ($\approx$1.0 G) were sufficiently narrow to permit a clear resolution of the hyperfine structure for the ^{107}Ag ($I=\frac{1}{2}$) and ^{109}Ag ($I=\frac{1}{2}$) isotopes, not only for the orientation $\vec{H}\|[111]$, but throughout the entire $(1\bar{1}0)$ plane. As shown in Fig. 1 (top and bottom), the observed first-derivative line shapes exhibited the symmetric form generally observed for EPR spectra of impurity ions in single crystals. These symmetric first-derivative line shapes were also present throughout the $(1\bar{1}0)$ plane. From the results presented in Ref. 24, it is known that near the static JT limit, the observed line shapes are more sensitive to the presence of intermediate JT effects than are straightforward measurements of the angular variation of the spectrum. This can easily be verified from a comparison of Figs. 2, 3, and 7 of Ref. 24. The line shapes shown here in Fig. 1 for Ag^{2+} in SrO do not exhibit any asymmetry of the type associated with an intermediate JT effect.

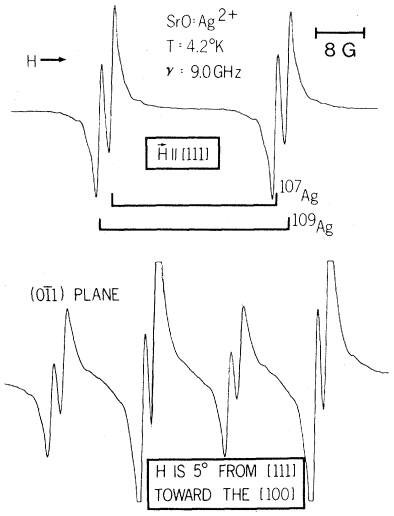

FIG. 1. Top: Low-temperature EPR spectrum of Ag^{2+} in an SrO single crystal with the applied magnetic field parallel to the [111] direction. The two silver isotopes are clearly resolved and identified as shown. The spectrum is in the first-derivative form. *Bottom*: The first-derivative EPR spectrum of Ag^{2+} in SrO obtained when the applied field is rotated away from the orientation $\vec{H}\|[111]$ by 5° in the $(1\bar{1}0)$ plane. Two groups of resolved ^{109}Ag and ^{107}Ag hyperfine lines are present with one group having an intensity twice that of the other.

With a sample temperature of 4.2 K an interesting orientation-dependent saturation phenomenon was observed in the tetragonally symmetric Ag^{2+} spectrum. With the applied magnetic field oriented parallel to a $\langle 111\rangle$ direction, it was necessary to apply power levels in excess of 10.0 mW in order to partially saturate the spectrum. As the applied magnetic field was rotated away from the orientation $\vec{H}\|\langle 111\rangle$ it was possible to saturate the resonance transitions at power levels, which became increasingly lower as $\vec{H}$ approached the orientation $\vec{H}\|\langle 100\rangle$. In particular, with $\vec{H}\|\langle 100\rangle$, the transitions corresponding to the magnetic field orientation lying parallel to the principal symmetry axis could be easily saturated with power levels as low as 0.01 mW. Although no attempt was made to measure the relaxation times as a function of applied magnetic field orientation, the above observations are consistent with an orientation dependent spin-lattice relaxation rate T_1 which is much longer at the orientation $\vec{H}\|\langle 100\rangle$ than at $\vec{H}\|\langle 111\rangle$. An expression for the direct process spin-lattice relaxation rate has been derived previously by Ham [see Eq. (2.6.2) of Ref. 1]. This result predicts an anisotropic relaxation rate and also predicts that T_1 should be relatively long for the orientation $\vec{H}\|\langle 100\rangle$. Our observations on the saturation behavior of the Ag^{2+} spectrum in SrO, although qualitative, are in agreement with the predicted behavior as noted above. As a result of these observations and the purity of the SrO:Ag^{2+} system relative to the presence of other impurity-ion spectra, it is apparent that this represents an ideal static JT system for a careful quantitative examination of the spin-lattice relaxation rates.

For the particular case of a system characterized by a pure static JT effect, it is necessary to observe a thermal averaging of the spectrum at elevated temperatures in order to substantiate the identification of the origin of the axial spectra as arising from a Jahn-Teller effect. In the absence of such an observation, the argument can justifiably be made that perhaps the tetragonal symmetry is simply a consequence of some associated defect in the host crystal. For Ag^{2+} in SrO, the

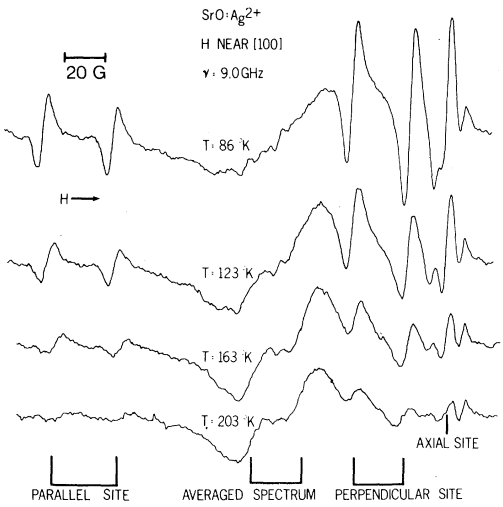

FIG. 2. Temperature variation of the Ag^{2+} EPR spectrum in an SrO single crystal with the applied magnetic field oriented near a [100] crystallographic direction. The two silver isotopes are not resolved in this temperature range. As the anisotropic "parallel" and "perpendicular" components decrease in intensity with increasing temperature, the "averaged" isotropic spectrum increases in intensity and resolution. An additional unknown center with ⟨111⟩ axial symmetry is located at the high-field side.

transition from the tetragonal symmetry spectra to the "averaged" spectrum was observed to take place over a broad temperature range, with the transition region extending from below 77 K to slightly above 203 K. As shown in Fig. 2, at a temperature of 86 K with the applied magnetic field oriented near a ⟨100⟩ direction, the "averaged" spectrum is already in evidence in the form of a single broad resonance. At 123 K, the intensity of the tetragonal symmetry spectra has decreased considerably, and the averaged spectrum is beginning to show a resolved Ag^{2+} hyperfine structure. (The lines are, of course, too broad at these temperatures to permit a resolution of the ^{107}Ag and ^{109}Ag isotope.) At a sample temperature of 203 K, the tetragonal components have almost disappeared and, as shown in Fig. 2, the averaged spectrum now consists of two reasonably well-defined, broad resonance lines. At 203 K, the averaged spectrum may be said to be "isotropic" in the sense that the magnetic field positions of the line centers do not change as a function of applied magnetic field orientation. The "averaged" lines do, however, exhibit a considerable anisotropy in the widths of the two component EPR transitions. This linewidth anisotropy persists to even higher temperatures when the tetragonal components can no longer be detected. The linewidth of the "averaged" components is a maximum at the orientation $\vec{H} \| \langle 100 \rangle$ and reaches a minimum value with $\vec{H} \| \langle 111 \rangle$. The spectrum for Ag^{2+} in SrO at 223 K, with $\vec{H} \| \langle 111 \rangle$, is shown in Fig. 3. At this temperature the tetragonal symmetry components can no longer be detected. A comparison between this spectrum and the "averaged" spectrum shown in Fig. 2 clearly shows the change in linewidth and the associated increased resolution of the composite (i.e., unresolved ^{107}Ag and ^{109}Ag) hyperfine structure which is obtained at the orientation corresponding to $\vec{H} \| \langle 111 \rangle$.

The g value and hyperfine structure parameter A of the high-temperature "averaged" Jahn-Teller spectrum should be related to the parameters $g_\parallel$, $g_\perp$, $A_\parallel$, and $A_\perp$ which describe the low-temperature "static" JT spectrum by the following expressions:

$$g_{av} = \tfrac{1}{3}(g_\parallel + 2g_\perp), \tag{6}$$

$$A_{av} = \tfrac{1}{3}(A_\parallel + 2A_\perp). \tag{7}$$

The g_{av} and A_{av} values experimentally determined at 223 K for Ag^{2+} in SrO with $\vec{H} \| [111]$ are listed in Table II together with values determined previously for Ag^{2+} in other hosts where the JT effect has been identified as static[31-33] (or quasistatic). The calculated values for g_{av} and A_{av} in Table II are determined using Eqs. (6) and (7) and the experimentally determined $g_\parallel$, $g_\perp$, $A_\parallel$, and $A_\perp$ which describe the low-temperature tetragonal spectra. The experimentally determined g_{av} value of 2.047 ± 0.002 agrees within the experimental error with the calculated g_{av} value of 2.049. The agreement between the "averaged" hyperfine parameters is not as a satisfactory, however. From the results presented in Fig. 2, there appears to be a slight diminution of the hyperfine splitting in the averaged spectrum between 123 and 203 K. Owing to the poor resolution of the hyperfine structure in the "averaged" spectrum at 123 K, it is difficult to determine with a high degree of certainty whether or not such an effect is present and, at the lower

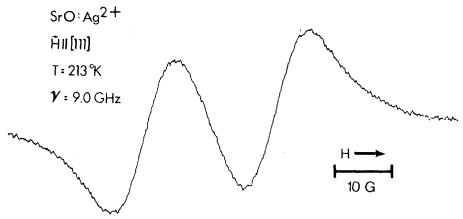

FIG. 3. "Averaged" Ag^{2+} EPR spectrum in SrO at a temperature of 213 K with $\vec{H} \| [111]$. The resolution of the hyperfine lines at this orientation is superior to that evident in Fig. 2 where $\vec{H}$ is near the [100] direction. Significant anisotropy in the line widths of the "averaged" spectrum persists after the anisotropic components of the Ag^{2+} low-temperature spectrum can no longer be detected.

TABLE II. Averaged Ag^{2+} parameters.

Host	T (K)	Expt. g_{av}	Expt. $^{107}A_{av}$ (10^{-4} cm^{-1})	Expt. $^{109}A_{av}$ (10^{-4} cm^{-1})	Calc. g_{av}	Calc. $^{107}A_{av}$ (10^{-4} cm^{-1})	Calc. $^{109}A_{av}$ (10^{-4} cm^{-1})
SrO[b]	223	2.047 ± 0.002	⟨21.6 ± 0.5⟩ [a]		2.049	24.8	28.8
CaO[b]	77	2.0760 ± 0.0005	23.3 ± 0.2	26.6 ± 0.2	2.076	23.8	27.8
CaO[c]	100	2.075	⟨25.6⟩ [a]		...	...	...
KCl[d]	300	2.09 ± 0.01	...	...	2.088	...	...
LiCl[e]	130	2.085 ± 0.002	...	...	2.085	...	...
NaCl[e]	200	2.092 ± 0.002	...	...	2.093	...	...

[a] The ^{107}Ag and ^{109}Ag isotopes could not be resolved experimentally at this temperature, and the quoted A-value therefore represents an effective "average" A_{av}-value for the two isotopes.
[b] This work.
[c] Reference 33.
[d] Reference 31.
[e] Reference 32.

temperatures, the increased resolution at the orientation $\vec{H} \| \langle 111 \rangle$ cannot be utilized to make more accurate measurements due to interference from the anisotropic tetragonal symmetry components of the Ag^{2+} spectrum. Unfortunately there is also a dearth of previously published data which would enable a comparison to be made between the experimental and calculated values of the hyperfine coupling constant for the "averaged" spectrum in static JT systems. From the data summarized in Table III of Ref. 1, it is apparent that for one of the three listed systems for which a comparison of this type can be made, the difference between the experimental and calculated values of A_{av} lies outside of the experimental error. This result and the result obtained in the present work for Ag^{2+} in SrO suggest that there is a possible additional temperature-dependent contribution to the hyperfine structure which may modify the applicability of Eq. (7). In contrast to this situation, the data listed in Table III of Ref. 1 indicate that the agreement between the experimental and calculated g values is generally quite good as it is in the present case of Ag^{2+} in SrO.

For Ag^{2+} in SrO, the observed three, generally inequivalent tetragonally symmetric spectra, the symmetric line shapes throughout a {110} plane, and the averaging at a relatively high temperature all serve to classify the SrO:Ag^{2+} system as a pure static Jahn-Teller case. The fact that $g_{\parallel}$ is greater than $g_{\perp}$ indicates that the A_2 level is the lowest vibronic singlet.

B. Ag^{2+} in CaO

The crystal growth procedure employed in the production of the silver-doped CaO samples was similar to that used for the SrO growth in that the starting material was in the carbonate form ($CaCO_3$). For the resulting CaO single crystals, however, the purity with respect to paramagnetic ions other than Ag^{2+} was not as high as for the SrO:Ag^{2+} specimens discussed in Sec. III A. The EPR spectrum obtained with a sample temperature of 77 K following the room-temperature uv irradiation of a typical silver-doped CaO crystal is shown in Fig. 4. In addition to an *isotropic* Ag^{2+} spectrum, an intense spectrum due to Mn^{2+} in a cubic symmetry site is evident. Fortunately, at liquid-helium temperatures, the Mn^{2+} spectrum could be saturated easily while the Ag^{2+} spectrum could be saturated only at considerably higher microwave power

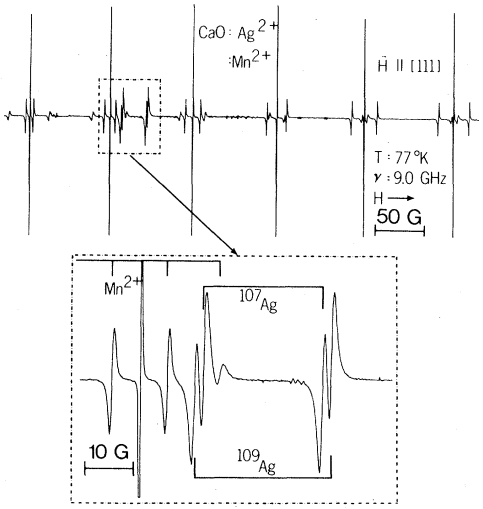

FIG. 4. EPR spectra present in a single crystal of silver-doped CaO at T = 77 K. In addition to the isotropic Ag^{2+} "averaged" spectrum, an intense spectrum due to Mn^{2+} in a cubic site is observed. At this orientation (i.e., $\vec{H} \| [111]$) one of the Mn^{2+} fine-structure lines interferes slightly with the low- field ^{107}Ag hyperfine line. (The first derivative of absorption is shown.)

levels, and accordingly, interference from the manganese spectrum could be minimized by operating the spectrometer at intermediate microwave power levels. The magnetic field region in which the isotropic Ag^{2+} spectrum appears at 77 K is shown using an expanded scale at the bottom of Fig. 4. The small resonance line which appears just slightly to the high-field side of the low-field ^{107}Ag hyperfine component is due to one of the $\frac{3}{2} \rightarrow \frac{5}{2}$ fine-structure lines of the second (counting from low field) Mn^{2+} hyperfine groups.

The Ag^{2+} spectrum observed at 77 K for the CaO host is significantly different from that found for Ag^{2+} in SrO at the same temperature in two essential respects: First, the anisotropic tetragonal symmetry spectral components found at 77 K (and clearly in evidence in Fig. 2 at 86 K) for Ag^{2+} in SrO were not detected at 77 K for divalent silver in CaO. Additionally, for CaO, the linewidths were sufficiently narrow at 77 K to permit a clear resolution of the ^{107}Ag and ^{109}Ag isotopes as shown in Fig. 4. These two significant differences already in evidence at 77 K are suggestive of the more fundamental differences exhibited by the results obtained at liquid-helium temperatures for the CaO and SrO:Ag^{2+} systems.

The EPR spectrum obtained at 1.3 K for Ag^{2+} in CaO with the magnetic field oriented parallel to a ⟨111⟩ crystallographic direction is shown in Fig. 5. This spectrum was obtained following a careful

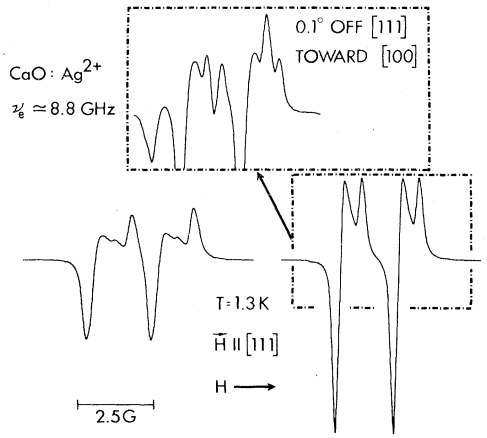

FIG. 5. EPR spectrum of Ag^{2+} in a CaO single crystal at $T = 1.3$ K, with $\vec{H} \| [111]$. The line shapes for the low-field hyperfine components are significantly different from those of the high-field components. The inset at the top of the figure illustrates the sensitivity of the line shape to magnetic field orientation. Each of the line-shape features including the protuberance at high field is observed to split as $\vec{H}$ is rotated away from $\vec{H} \| [111]$. These line shapes represent one characteristic of the intermediate Jahn-Teller effect. (The spectra are in the form of the first derivative of absorption.)

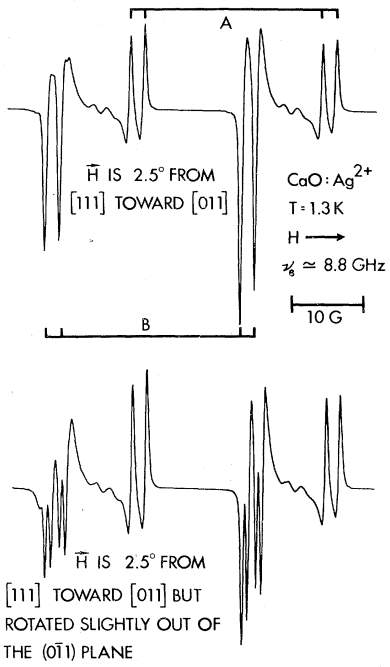

ORIENTATION DEPENDENCE OF Ag^{2+} SPECTRA IN CaO

FIG. 6. *Top*: EPR spectrum of Ag^{2+} in a CaO single crystal with $\vec{H}$ oriented 2.5° from the [111] direction in the (1$\bar{1}$0) plane. The asymmetric first derivative line shapes resemble those observed for systems characterized by the "pure dynamic" Jahn-Teller effect. These line shapes should be compared with those shown at the bottom of Fig. 1 for Ag^{2+} in SrO. Bottom: When the applied magnetic field is rotated slightly out of the (1$\bar{1}$0) plane, each of the components labelled "*B*" in the top part of the figure splits into two components. This shows that there are three generally inequivalent spectra present.

in situ orientation of the crystal as described previously. The inset at the top of Fig. 5 indicates the degree of sensitivity of the line shape to magnetic field orientation. A comparison of this line shape with that shown at the top of Fig. 1 for SrO:Ag^{2+} with $\vec{H} \| [111]$ shows that the line shapes for these two systems are fundamentally very different. Accordingly, owing to the seemingly highly unusual nature of this feature at the time of its discovery, the true form of the line shape for CaO:Ag^{2+} was repeatedly verified by *in situ* orientations of numerous silver-doped CaO crystals.

Additional significant differences between the CaO:Ag^{2+} and SrO:Ag^{2+} systems at 1.3 K are evident when the magnetic field is not applied at the orientation $\vec{H} \| [111]$. The spectrum obtained when the applied magnetic field is oriented 2.5° away from the [111] direction in the (1$\bar{1}$0) plane is shown at the top of Fig. 6. At this orientation the spec-

trum consists of two groups of ^{107}Ag and ^{109}Ag hyperfine lines, denoted by "*A*" and "*B*" in Fig. 6, plus a weak isotropic hyperfine group, which is evident between the components of the *A* and *B* anisotropic spectra. The group labeled *B* is seen to have approximately twice the intensity of the group denoted as *A*. A comparison of the line shape observed at a general orientation for the anistropic components of the Ag^{2+} spectrum in SrO (as shown at the bottom of Fig. 1) with those evident in Fig. 6 shows that the line shapes for the two hosts are completely different. For Ag^{2+} in CaO, the line shapes resemble those found previously for systems characterized by a low-temperature dynamic JT effect.[15-19] When the applied magnetic field is rotated out of the $(1\bar{1}0)$ plane, each of the *B* components of the spectrum splits into two components, which shows that there are three generally inequivalent spectra present for the CaO:Ag^{2+} system. A careful examination of the angular variation giving particular attention to the establishment of the equivalence of the $g_\perp$ values in the $(1\bar{1}0)$ plane also shows that, within experimental error, the spectra exhibit tetragonal symmetry. The angular variation of the spectra observed for Ag^{2+} in CaO is therefore consistent with that associated with Eqs. (4). The effective Hamiltonian parameters $g_\parallel$, $g_\perp$, $A_\parallel$, and $A_\perp$ for CaO:Ag^{2+} were determined using the identical computer technique described previously for Ag^{2+} in SrO, and these parameters are listed in Table I.

The spectrum found for Ag^{2+} in CaO is, therefore, similar to that observed for the SrO:Ag^{2+} system in that both systems are characterized by three generally inequivalent, tetragonal symmetry spectra. The spectra for the two hosts appear to be very different, however, on the basis of a line-shape comparison for a general applied field orientation as well as for the orientation $\vec{H}\parallel\langle 111\rangle$.

As previously discussed, the unusual line shapes of the type observed for Ag^{2+} in CaO with $\vec{H}\parallel\langle 111\rangle$ are an important characteristic of the intermediate JT effect. Using a computer technique to diagonalize the matrix of strain and tunneling for the ψ_1, ψ_2, and ψ_3 manifold of states [i.e., Eq. (2)] it is possible to compute the EPR line shapes as a function of $\bar{\delta}/3\Gamma$, and, therefore by fitting an observed line shape, to determine this ratio for a given system. For Ag^{2+} in CaO, the value determined for $g_\parallel$ is greater than that found for $g_\perp$ and this is consistent with having the A_2 vibronic singlet nearest the ^2E_g ground state.[1] Accordingly, the matrix of strain and tunneling to be diagonalized is given by Eq. (2) with only the lower values of the signs. For the line shapes observed at a frequency of approximately 8.8 GHz, the expectation values of the Zeeman and hyperfine interactions were computed using the eigenvectors which resulted from the diagonalization of Eq. (2) (i.e., both interactions were treated by perturbation theory and were not included in the matrix prior to the diagonalization).

For the magnetic field orientation $\vec{H}\parallel\langle 111\rangle$, the various contributions to the spectrum due to the random nature of the strains were summed over an ensemble of sites having a uniform distribution of ϕ values (where $\tan\phi = e_\epsilon/e_\theta$) between 0 and 2π. A Gaussian distribution of random strain splittings was employed, and the spectra from each Kramers doublet were weighted by a Boltzman factor appropriate to the assumed temperature. (The details of this procedure are treated in Ref. 24.) The results obtained after the ratio of $\bar{\delta}/3\Gamma$ had been adjusted until the line shapes of the calculated and computed spectra were as similar as possible are shown in Fig. 6. Since the line shapes are identical for the ^{109}Ag and ^{107}Ag isotopes, the calculations were performed only for the ^{109}Ag isotope.

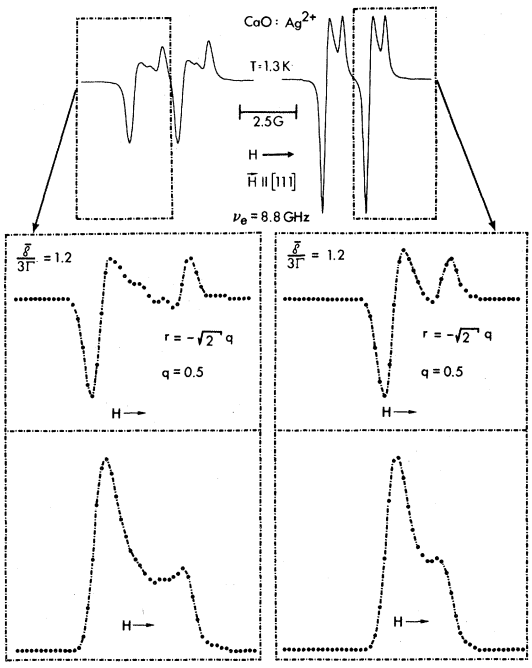

FIG. 7. *Top*: The experimental *X*-band line shapes of Ag^{2+} in a CaO single crystal shown in the first derivative of absorption form. The applied magnetic field is parallel to the [111] direction. *Middle*: The first-derivative line shapes computed using a value for $\bar{\delta}/3\Gamma$ of 1.2. Assumptions that $r = -\sqrt{2}\,q$, and $q = 0.5$ have been made. The magnetic field scale is larger than that shown for the experimentally determined line shapes. *Bottom*: The calculated absorption line shapes, whose first derivative are shown directly above, are presented. Both the absorption line shapes and their corresponding first derivatives were computed by a repetitive diagonalization of the matrix of strain and tunneling appropriate to the A_2, $E_{g\theta}$, $E_{g\epsilon}$ manifold of states.

A comparison of the experimental results reproduced at the top of Fig. 7 with the computed first-derivative curves given in the middle of the figure, shows that an excellent fit is obtained when $\bar{\delta}/3\Gamma$ equals 1.2. (The magnetic field scale for the computed first-derivative line shape is slightly larger than that of the experimental line shapes in Fig. 7. A point-by-point computer plot was employed in these calculations, and it was necessary to use a slightly expanded scale in order to show the particular detail present in the line shape of the low-field hyperfine component.) The corresponding calculated absorption line shapes for each ^{109}Ag hyperfine component are shown at the bottom of Fig. 7.

The line shapes observed at a frequency of 23 GHz for Ag^{2+} in CaO with $\vec{H} \| [111]$ are shown at the top of Fig. 8. When a calculation of the line shapes identical to that described above was performed with $\bar{\delta}/3\Gamma = 1.2$ for a frequency of 23 GHz, the resulting fit was not good. In fact, using the assumptions previously noted, in order to obtain agreement between the experimental and computed line shapes at 23 GHz it is necessary to increase the value of $\bar{\delta}/3\Gamma$ to 4.5. A value of $\bar{\delta}/3\Gamma = 4.5$ would, of course, correspond to a Jahn-Teller effect which has a more "static" character than that associated with the value of $\bar{\delta}/3\Gamma = 1.2$, as calculated from the results at 8.8 GHz. It has been pointed out previously by Ham,[1] that a strong Zeeman interaction can have the effect of stabilizing a JT system to produce a more static Jahn-Teller effect. Accordingly, based on this and the results described above, the conclusion was made that at 23 GHz the Zeeman interaction is no longer negligible relative to the random strain splitting. Therefore, in order to perform a proper calculation of the line shapes observed at 23 GHz, it was necessary to diagonalize Eq. (2) or its equivalent with the addition of the appropriately transforming Zeeman terms.

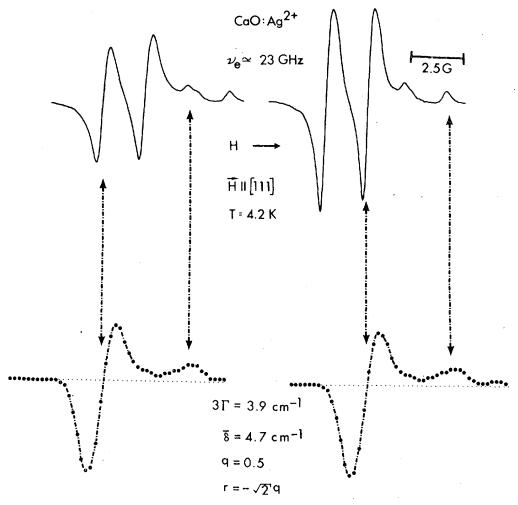

FIG. 8. Top: The experimental line shapes at 23 GHz for Ag^{2+} in a CaO single crystal at a temperature of 4.2 K. In contrast to the line shapes obtained at *X* band (8.8 GHz), the low- and high-field hyperfine components have the same form in the first derivative presentation. *Bottom*: The calculated first-derivative line shapes at 23 GHz. At this frequency the Zeeman interaction must be explicitly included in the matrix of strain and tunneling prior to the diagonalization. This procedure determines the value of 3Γ as 3.9 cm^{-1}.

The details of the calculation including the Zeeman interaction are presented in the Appendix. In carrying out this calculation, the dynamic basic states $\psi_{g\theta}$, $\psi_{g\epsilon}$, and ψ_{A_2} were used and a coordinate transformation was performed to bring the z axis parallel to a $\langle 111 \rangle$ crystallographic direction (i.e., parallel to the applied magnetic field at the orientation $\vec{H} \| \langle 111 \rangle$). The matrix elements which were off-diagonal in the electronic spin were then small relative to the diagonal terms, so that it was necessary to diagonalize only the 3×3 matrices which were diagonal in terms of spin. The off-diagonal elements were then treated by perturbation theory. A Gaussian distribution of the strain magnitudes was employed and the strain distributed between components as described in Ref. 24. The spectra arising from the various levels were weighted by the appropriate Boltzmann factor. The line shape resulting from this calculation with a frequency of 23 GHz is shown at the bottom of Fig. 8. The line-shape agreement is apparently quite good. Although the line shapes for the low- and high-field hyperfine components were significantly different at 8.8 GHz (see Fig. 6), the line shapes are found to be equivalent for the two components at 23 GHz (Fig. 8) owing to the increased role of the Zeeman interaction, and the results of the calculation described above verify this effect.

Since the strength of the Zeeman interaction is known at 23 GHz, the ratio of the Zeeman to tunneling interaction then uniquely determines the tunneling splitting 3Γ, which is found to be 3.9 cm^{-1}. If the line shape with $\vec{H} \| [111]$ for the 9-GHz spectrum is then computed under these conditions, the line-shape fit shown in Fig. 7 is duplicated. Accordingly, the 9-GHz spectrum is not affected by the Zeeman interaction, and the ratio $\bar{\delta}/3\Gamma = 1.2$, determined at 9 GHz, is the correct one. This ratio together with the value of 3.9 cm^{-1}, determined for 3Γ, fixes the value of the strain splitting $\bar{\delta}$ as 4.7 cm^{-1}. The ability to determine 3Γ and $\bar{\delta}$ independently more than justifies the additional effort required to carry out a line-shape calculation with the inclusion of the Zeeman interaction. It should be possible to exploit the intermediate Jahn-Teller effect in the CaO:Ag^{2+} system by means of

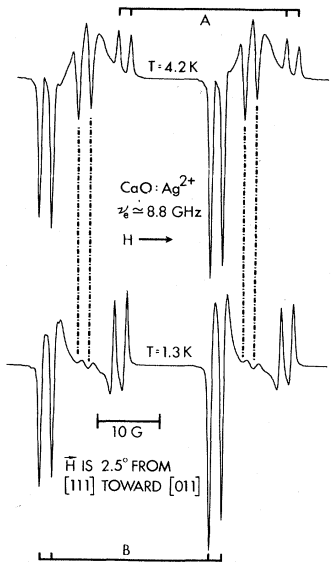

FIG. 9. Variation at low temperature of the relative intensities of the isotropic and anisotropic Ag^{2+} spectra in CaO. The averaging of the anisotropic components occurs rapidly in this temperature range.

this calculation in order to study the various random strain splittings which could result from such factors as different crystal growth techniques, heavy neutron irradiations, etc., and investigations of this type are planned as an extension of the work reported here.

The presence of the isotropic spectrum shown in Fig. 4 for Ag^{2+} in CaO at 77 K shows that the thermal averaging of the anisotropic A and B components in Fig. 5 must occur relatively rapidly with increasing temperature between 1.3 and 77 K. An indication of the rate of this averaging with increasing temperature is given in Fig. 9, which shows the anisotropic A and B components and the isotropic spectra (as connected by the dotted lines) at 1.3 and 4.2 K. Although the temperature difference of 2.9 K represents a very narrow temperature range, the intensity of the isotropic components relative to, for example, the A anisotropic components has changed by a factor of approximately 50. The low-temperature averaging of the Ag^{2+} spectrum in CaO has been investigated previously by Müller and Berlinger[34] using silver-doped CaO powder samples. Their results show that the temperature averaging of the anisotropic components is essentially complete at a temperature of 25 K.

The spin-Hamiltonian constants g_{av} and A_{av} which describe the isotropic Ag^{2+} spectrum shown in Fig. 4 have been determined, and the results are listed in Table II along with the corresponding values which were calculated using Eqs. (6) and (7) and the effective Hamiltonian parameters given in Table I. For the CaO:Ag^{2+} system, exact agreement between the g_{av} value determined experimentally at 77 K and the calculated g_{av} value is obtained. The experimental and calculated values of A_{av} for the ^{107}Ag and ^{109}Ag isotopes, although reasonably close to each other, still differ by an amount which lies outside of the experimental error. The agreement between the experimental and calculated values of A_{av} for Ag^{2+} in CaO is, however, much better than that obtained for the SrO:Ag^{2+} system treated earlier. There is, of course, a significant difference in the temperature at which the measurements on the isotropic spectra for Ag^{2+} in CaO and SrO were made. A simple average of the ^{107}Ag and ^{109}Ag hyperfine parameters yields a value of $A_{av} = 25.0 \pm 0.2 \times 10^{-4}$ cm^{-1}, which compares favorably with the value of $A_{av} = 25.6 \times 10^{-4}$ cm^{-1}, which was obtained[33] using a powder sample at a temperature of 100 K.

According to the criteria discussed in Sec. II of the present work, the various features of the spectra observed for Ag^{2+} in CaO all serve to characterize this system as a quasistatic Jahn-Teller case. This type of Jahn-Teller effect occurs, as previously noted, when the value of the ratio of the random strain splitting $\bar{\delta}$ to tunneling splitting 3Γ is somewhat smaller than that necessary to place the system in the pure static JT limit. From the results presented in Ref. 24, it is known that a value of $\bar{\delta}/3\Gamma$ somewhat greater than 5 is required in order to obtain the characteristics of the pure static JT effect. The value of $\bar{\delta}/3\Gamma = 1.2$ which has been calculated from the line-shape analysis is therefore entirely consistent with the quasistatic JT classification as applied to Ag^{2+} in CaO.

C. Ag^{2+} in MgO

Arc-fusion growth of the Ag^{2+}-doped MgO single-crystal samples investigated here was carried out using starting material in the form of magnesium oxide, rather than the carbonate form which was used for the growth of both SrO and CaO. An irradiation using a short wavelength uv lamp was again necessary in order to observe the Ag^{2+} spectrum.

The EPR spectrum obtained for Ag^{2+} in MgO at a temperature of 1.3 K with the applied magnetic field parallel to a [111] direction is shown in Fig. 10. At this temperature and orientation, the linewidth is sufficiently narrow to permit an excellent resolution of the spectra due to the ^{107}Ag and ^{109}Ag isotopes as shown in the figure. The line shapes which are evident in Fig. 10 were obtained follow-

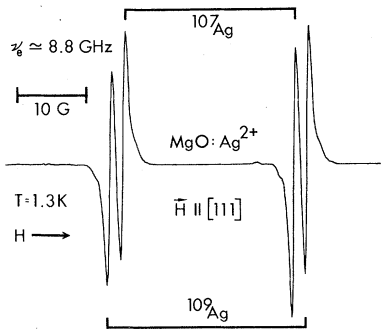

FIG. 10. EPR spectrum observed for Ag^{2+} in MgO at $T = 1.3$ K, with the applied magnetic field oriented parallel to the [111] direction. At this orientation the line shapes are similar to those shown at the top of Fig. 1 for Ag^{2+} in SrO.

ing a careful *in situ* orientation of the single-crystal sample. A comparison of these line shapes with those found for the spectrum of Ag^{2+} in SrO, as shown at the top of Fig. 1, indicates that the line shapes for Ag^{2+} in MgO and SrO are quite similar at 1.3 K with $\vec{H} \| [111]$. Any further similarity of the spectra for the MgO:Ag^{2+} and SrO:Ag^{2+} systems vanishes immediately, however, when the applied magnetic field is rotated away from the orientation $\vec{H} \| [111]$ in a $(1\bar{1}0)$ plane. The spectra obtained when the applied field is rotated 16° away from the orientation $\vec{H} \| [111]$ towards the [011] direction and 12° away from $\vec{H} \| [111]$ toward the [100] direction are shown in Fig. 11. The following characteristics of the spectra obtained at these orientations are immediately apparent: First, the linewidth of all of the components has broadened (relative to the width at $\vec{H} \| [111]$) to the point where it is no longer possible to resolve the two silver isotopes. Second, the spectrum now consists of two groups of two lines, and both groups exhibit asymmetric line shapes. Finally, the linewidth for one of the groups of two lines is considerably narrower than that of the other and the apparent intensity (i.e., the peak-to-peak height in the first-derivative presentation) of this narrow group is larger than that of the broad group by a factor of approximately 4. The "narrow" two-line group is observed to move from the high-field side of the magnetic field position of the spectrum with $\vec{H} \| [111]$ to the low-field side of this position as the applied field is rotated from the orientation $\vec{H} \| [100]$ to $\vec{H} \| [110]$. When the applied magnetic field is rotated out of the $(1\bar{1}0)$ plane, neither the narrow nor the broad two-line spectra are observed to split further into two components. Therefore, in contrast to the spectra found for Ag^{2+} in SrO and CaO, the spectrum observed for the MgO:Ag^{2+} system does not consist of three generally inequivalent components with tetragonal symmetry.

The experimentally determined angular variation in the $(1\bar{1}0)$ plane is shown in Fig. 12, where the experimental points are indicated by the open circles. This angular variation appears to be identical to the type of angular variation previously observed for systems characterized by a pure dynamic Jahn-Teller effect[15-19] (in particular, the angular variation in Fig. 12 can be compared to that shown in Fig. 4 of Ref. 18). In spite of this apparent similarity, the angular variation exhibits some significant quantitative differences with respect to that appropriate to a pure dynamic JT system. These differences become evident when an attempt is made to account for the complete experimentally determined angular variation by using Eq. (3) of Ref. 18, which is only appropriate to the pure dynamic JT case. Using the measured values for the magnetic field positions of the "narrow" components of the spectrum at various applied field orientations, a least-squares fit was made to Eq. (3) of Ref. 18, and the effective Hamiltonian parameters g_1, qg_2, A_1, and qA_2 listed in

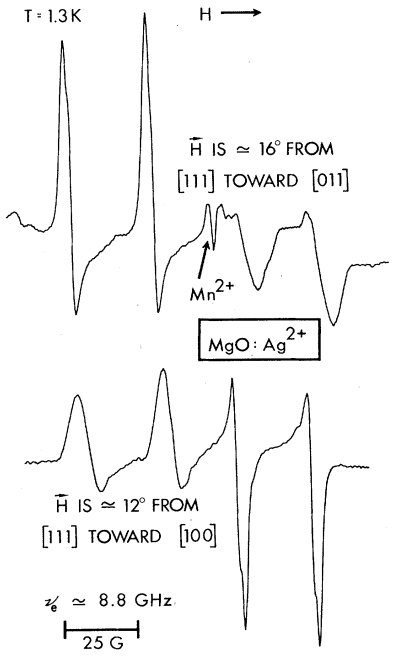

FIG. 11. EPR spectra of Ag^{2+} in MgO observed when the applied magnetic field is rotated away from the [111] direction toward the [011] (top) and [100] (bottom) directions. The line shapes resemble those found previously for systems characterized by a pure dynamic JT effect. The "narrow" hyperfine set moves from the high-field side of the magnetic field position $\vec{H} \| [111]$ to the low-field side of this position as the magnetic field is rotated from $\vec{H} \| [100]$ to $\vec{H} \| [011]$ in a $(1\bar{1}0)$ plane.

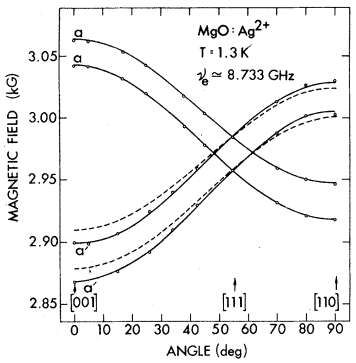

FIG. 12. Experimentally determined angular variation fro the spectrum of Ag^{2+} in MgO is indicated by the open circles. The solid curves represent the fit to this angular variation which was calculated from a diagonalization of the matrix of strain and tunneling for the A_2, $E_{g\theta}$, and $E_{g\epsilon}$ manifold of states. This fit corresponds to a value of $\bar{\delta}/3\Gamma = 0.13$. The dotted lines represent the angular variation calculated using Eq. (3) of Ref. 18 which is only valid for the pure dynamic JT case.

Table I were determined. These effective Hamiltonian parameters were then used in Eq. (3) of Ref. 18 to calculate the angular variation for both the "narrow" and "broad" components. For the narrow components (i.e., those components having a high-field extreme at the orientation $\vec{H} \| [100]$ and a low-field extreme at $\vec{H} \| [110]$), the resulting calculated angular variation is indicated by the solid lines labeled a and a in Fig. 12, and the agreement with the experimental points is excellent. The angular variation calculated for the broad components using the same effective Hamiltonian parameters is indicated by the dotted lines in Fig. 12. As is evident in the figure, these lines do not fit the experimental points which were determined for the broad components of the spectrum. Therefore, although the EPR spectrum of Ag^{2+} in MgO is characterized by an angular variation which closely resembles that of a pure dynamic system, one set of components has been selectively broadened and shifted. This type of selective shift and broadening has been observed previously in the optically-detected EPR spectrum for an excited ^2E state of Eu^{2+} in CaF_2.[20,21] The effect arises when the first-excited vibronic singlet state is sufficiently close to the ^2E ground vibronic level so that perturbations via the random strain and Zeeman interaction can couple the two states. This coupling then produces the type of progressive changes in the angular variation that are illustrated in Fig. 3 of Ref. 24. By carrying out a calculation identical to that described in Sec. III B for the X-band Ag^{2+} spectrum in CaO (i.e., the calculation which does *not* include the Zeeman interaction in the matrix diagonalization) it is possible to adjust the value of $\bar{\delta}/3\Gamma$ until the computed and experimental values of the magnetic field positions for the broad components of the MgO:Ag^{2+} spectrum with $\vec{H} \| [100]$ coincide. (Since the qg_2 is positive, the shift of the component which is at low field with $\vec{H} \| [100]$ identifies the first-excited singlet as the A_2 level. See Table I of Ref. 24.) The value of $\bar{\delta}/3\Gamma$ determined by this procedure is given by $\bar{\delta}/3\Gamma = 0.13$. This value of $\bar{\delta}/3\Gamma$ can then be used to calculate the complete angular variation of both the broad and narrow spectral components in the $(1\bar{1}0)$ plane. The results of this calculation are indicated by the solid curves a and a' in Fig. 12, and the complete angular variation in the $(1\bar{1}0)$ plane is now described.

The temperature dependence of the isotropic Ag^{2+} spectrum in MgO between 2.0 and 4.2 K is shown in Fig. 13. At 4.2 K, the isotropic spectrum has a relatively high intensity in comparison with the anisotropic portion of the spectrum. As the temperature decreases, the intensity of the isotropic resonance lines decreases as a nonlinear function of the temperature. This rate of change in the in-

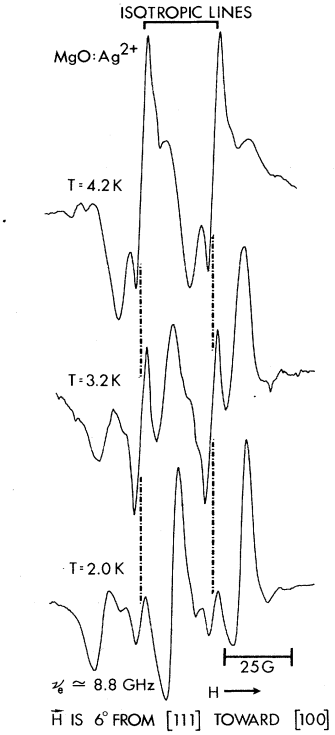

FIG. 13. Temperature variation of the isotropic and anisotropic components of the spectrum of Ag^{2+} in MgO between 2.0 and 4.2 K. The rate of increase of intensity of the isotropic components with increasing temperature is significantly greater than that found previously for pure dynamic JT systems. The isotropic components are indicated by the dashed lines.

tensity of the isotropic lines is much greater than that observed previously for systems characterized by the limiting case of the pure dynamic Jahn-Teller effect.[15-19] The isotropic spectrum observed for pure- or quasidynamic JT systems can result either from thermal population of the first-excited vibronic singlet (for MgO:Ag^{2+}, the A_2 singlet would be thermally populated) or from averaging by relaxation. The various criteria for distinguishing between these two possible origins of the isotropic spectrum have been discussed in detail previously in Ref. 24. Since, in the case of Ag^{2+} in MgO, the A_2 singlet is sufficiently close to the ground ^2E vibronic level to be coupled to this state via the strain and Zeeman interactions, and as a result of the previously noted large temperature variation in the intensity of the isotropic lines, it is reasonable to assume that thermal population of the A_2 level is responsible for a significant contribution to the intensity of the isotropic spectrum. Using this assumption and the functional form for the variation of the intensity given by $\exp(-3\Gamma/kT)$, it is possible to calculate a value for 3Γ from the observed integrated intensity of the isotropic lines between 4.2 and 1.3 K. A value of $3\Gamma = 4.8$ cm^{-1} is obtained from this calculation. The average strain splitting can then be calculated from this result and the previously determined value of $\bar{\delta}/3\Gamma = 0.13$. The resulting value for $\bar{\delta}$ is 0.62 cm^{-1}. Since it was not possible to accurately determine what fraction of the isotropic spectrum might be due to averaging by relaxation, the value of $3\Gamma = 4.8$ cm^{-1} must be assumed to be an approximate result.

The observed angular variation of the Ag^{2+} spectrum in MgO, the line shapes and line-shape variations, and the rapid averaging of the spectrum with increasing temperature all serve to classify the MgO:Ag^{2+} system as a quasidynamic Jahn-Teller case.

IV. DISCUSSION

The asymmetric line shapes observed for the CaO:Ag^{2+} system with the applied magnetic field oriented parallel to a ⟨111⟩ crystallographic direction represent one of the most interesting manifestations of the intermediate Jahn-Teller effect. Similar line-shape effects have been observed previously for Cu^{2+} in CaO, and the ability to calculate in detail the line shapes observed for these two systems provides a firm validation of the applicability of the three-state formalism described in Sec. II of this work. Physical insight into the nature of the origin of the line shapes observed for the orientation $\vec{H} \parallel \langle 111 \rangle$ may be obtained via the following considerations: For a system characterized by a "pure" dynamic JT effect, the g value corresponding to the orientation $\vec{H} \parallel \langle 111 \rangle$ is related to g_1 and qg_2 by the following equation:

$$g = [g_1^2 + \tfrac{1}{2}(qg_2)^2]^{1/2}. \tag{8}$$

For a "pure" static JT, system the equivalent relation is

$$g = [g_1^2 + 2(qg_2)^2]^{1/2}. \tag{9}$$

Generally the condition $g_1 \gg qg_2$ is satisfied and, in this event, the g values obtained from Eqs. (8) and (9) above are slightly different for the two limiting cases at the $\vec{H} \parallel \langle 111 \rangle$ orientation. For a system exhibiting intermediate JT effects, the intensity of the transitions at this orientation is effectively distributed between the positions associated with the g values for the limiting cases as noted above. The progressive change in the distribution of the intensity for intermediate JT cases (in the absence of a hyperfine interaction) has been illustrated in Figs. 6 and 7 of Ref. 24 as a function of $\bar{\delta}/3\Gamma$. These results indicate that the intensity is equally distributed between the "static" and "dynamic" g-value positions when $\bar{\delta}/3\Gamma$ is slightly larger than 0.5. For the case of Ag^{2+} in CaO, the low-field portion of the line as shown in Fig. 5 exhibits the greatest intensity and this is consistent with a more static intermediate JT effect and with the corresponding calculated value of $\bar{\delta}/3\Gamma = 1.2$. The ability to make a determination of $\bar{\delta}/3\Gamma$ by fitting line shapes of this type, even when deviations in the angular variation of a quasistatic JT spectrum cannot be detected experimentally, obviously represents an important source of information which is not available from EPR measurements made on systems in the limiting pure static case.

Measurements of the ratio $\bar{\delta}/3\Gamma$ and, in particular, an accurate independent determination of $\bar{\delta}$ and 3Γ (such as that performed here for Ag^{2+} in CaO) can provide a relatively complete characterization of the JT effect in a given system especially when such results are combined with those obtained from Raman scattering studies of the type reported by Guha and Chase.[28] Measurements of the separations of the excited vibronic levels by Raman scattering techniques permit a determination to be made of the relative contributions of the JT linear coupling and warping terms.

When an independent measurement of 3Γ and $\bar{\delta}$ is combined with the results of a determination of the strain coupling coefficient V_2 which appears in Eq. (3), it is possible to calculate directly the average value of the random tetragonal symmetry strain responsible for splitting the ground ^2E vibronic level. The strain coupling coefficient has been determined in Ref. 28 for Cu^{2+} in CaO by means of an applied external stress with the result $V_2 = 2.6 \times 10^4$ cm^{-1}. From the ratio $\bar{\delta}/3\Gamma = 0.67$

determined in Ref. 23 and the tunneling splitting of $3\Gamma = 4$ cm^{-1},[28] we obtain a value of 2.7 cm^{-1} for the average random strain splitting $\bar{\delta}$. These results can then be used in Eq. (3) to determine a value of 0.93×10^{-4} for the "average" random strain $(e_\theta^2 + e_\epsilon^2)_{av}^{1/2}$ in the CaO:Cu^{2+} case. Using the same value of V_2 and the result that for Ag^{2+} in CaO, $\bar{\delta} = 4.7$ cm^{-1}, it is possible to calculate an approximate value for $(e_\theta^2 + e_\epsilon^2)_{av}^{1/2}$ of 1.5×10^{-4}. Both of these values are listed in Table III along with other parameters appropriate to systems exhibiting intermediate JT effects. The above values of 0.93×10^{-4} and 1.5×10^{-4} determined for the average residual strain compare favorably with the value of 2×10^{-4} which was found by Stoneham[35] from an analysis of Fe^{2+} EPR linewidths in the alkaline-earth oxide MgO. Additional work by Stoneham[36] indicates that for the alkaline-earth oxides (and in particular for MgO), residual strains of the same order as those noted above can result from a dislocation density of 10^6 cm/cc or from point defects in a concentration of 70 ppm. It would be desirable to determine an accurate value of the strain coupling coefficient V_2 for the CaO:Ag^{2+} system by means of a calibration based on the application of a known applied stress. The resulting value of V_2 could then be used to perform quantitative studies of changes in the residual strains in CaO as a function of sample treatments such as neutron irradiation, annealing and quenching, ion implantation, etc. Such an investigation would, of course, involve a determination of values of $\bar{\delta}$ and 3Γ corresponding to the different magnitudes of the residual strain, and this determination would be carried out using the techniques discussed in the Appendix.

It should be noted that the calculations of various features of the intermediate JT effect as reported here have been performed using a value of 0.5 for the reduction factor q. This choice is justified by means of the following considerations: A value of $\hbar\omega = 330$ cm^{-1} has been calculated in Ref. 23 for the CaO host. Using this value and our value of $3\Gamma = 3.9$ cm^{-1} for Ag^{2+} in CaO, we determine that for this system the ratio $3\Gamma/\hbar\omega$ is equal to 0.01. Assuming linear JT coupling, this corresponds to a value for $E_{JT}/\hbar\omega$ of 42. For strong linear JT coupling, q is given by the expression $q \approx 1/2[1 + (\hbar\omega/4E_{JT})^2]$, and accordingly $q \approx \frac{1}{2}$ for Ag^{2+} in CaO. A similar argument can be made for the MgO:Ag^{2+} system where $3\Gamma = 4.8$ cm^{-1} and $E_{JT}/\hbar\omega \approx 40$. An examination of Eq. (2.3.44) in Ref. 1 shows that q should be 0.5 for all values of $E_{JT}/\hbar\omega \gtrsim 2$. Williams *et al.*[37] have shown that q and r are related by the expression

$$r = -q(1 - 3\epsilon)\sqrt{2} ,$$

when the linear JT coupling is strong, and, additionally, they have calculated values for ϵ as a function of the ratio of warping to linear JT coupling. Their results show that ϵ decreases rapidly as the warping increases and that $r = -\sqrt{2}q$ for large warping. For both the CaO:Ag^{2+} and MgO:Ag^{2+} systems, the Jahn-Teller coupling is not purely linear since the experimental results indicate that the ground ^2E level is only coupled to one excited vibronic singlet and, therefore the relation $r = -\sqrt{2}q$ should be valid. A quantitative value for the splitting of the A_2 and A_1 vibronic singlet levels cannot be deduced from EPR measurements such as those reported here, but this value may be determined by employing the Raman scattering technique.

It is possible to relate the effective Hamiltonian parameters g_1, g_2, A_1, A_2 to the ratio of the spin-orbit coupling λ to the cubic crystal-field splitting $\Delta = 10Dq$ by the following expressions, which are valid when the spin-orbit coupling is small relative to the crystal-field interaction[1]:

$$\begin{aligned} &g_1 = 2.0023 - 4\lambda/\Delta , \quad g_2 = -4\lambda/\Delta = g_1 - 2.0023 , \\ &A_1 = (-2\mu_B\mu\langle r^{-3}\rangle/I)(\kappa + 4\lambda/\Delta) , \\ &A_2 = (-2\mu_B\mu\langle r^{-3}\rangle/I)(\tfrac{4}{7} + 34\lambda/7\Delta) , \end{aligned} \tag{10}$$

Here κ is the Fermi contact parameter, $\langle r^{-3}\rangle$ represents the one-electron expectation value of r^{-3}, and μ is the nuclear magnetic dipole moment. Values of g_1, qg_2, A_1, and qA_2 have been calculated from Eqs. (5) and the parameters listed in Table I for Ag^{2+} in SrO and CaO. The calculated results for g_1 and qg_2 are listed in Table III along with the g_1 and qg_2 directly measured for Ag^{2+} in MgO.

The usual procedure for determining the value of q for these systems is to calculate g_2 from the measured value of g_1 using Eqs. (10) and to employ this value of g_2 in order to calculate q from the measured value of qg_2. If this procedure is employed using the values g_1 and qg_2 obtained as noted above, we obtain the q values for Ag^{2+} in SrO, CaO, and MgO, which are listed in Table III. It is immediately apparent that not only are all of the q values significantly greater than 0.5, but that the largest q value is obtained for the static JT system while the smallest value is found for the quasidynamic case. This trend is exactly opposite to the expected behavior since q values greater than 0.5 should only be found for those cases where the JT coupling is weak. In Ref. 1, the $g_\parallel$ and $g_\perp$ values have been tabulated for six different systems in which the JT impurity is either Cu^{2+} or Ag^{2+} (i.e., a d^9 configuration) and for which the JT effect has been identified as static. If we use a procedure identical to that described above to calculate q for these static sys-

TABLE III. Parameters for Ag^{2+} and Cu^{2+} in MgO, CaO, and SrO single crystals.

System	Lowest vibronic singlet	3Γ (cm^{-1})	$\bar{\delta}$ (cm^{-1})	$\frac{\bar{\delta}}{3\Gamma}$	g_1	qg_2	q	Random strain $(e_\theta^2+e_\varepsilon^2)_{av}^{1/2}$	κ	Reference
$SrO:Ag^{2+}$	A_2	...	...		2.049.[e]	+0.032[e]	0.682	...	4.5	a
$CaO:Ag^{2+}$	A_2	3.9	4.7	1.2	2.076[e]	+0.045[e]	0.610	1.4×10^{-4}[g]	2.7	a
$MgO:Ag^{2+}$	A_2	4.8	0.62	0.13	2.0998	+0.0563	0.577	...	1.3	a
$CaO:Cu^{2+}$	A_1	$\simeq4$	2.7	0.67	2.2211	+0.122	0.557	0.93×10^{-4}	0.003	b
$CaO:Cu^{2+}$	...	$\simeq4$ 3.25[d]	...	$\simeq1$	...	...	...	...	...	c
$MgO:Cu^{2+}$	A_2[f]		...	...	...	...	...	...	...	b

[a] This work.
[b] Reference 23.
[c] Reference 28.
[d] The value of 3.25 cm^{-1} was calculated in Ref. 28 based on the results obtained for the higher-lying vibronic levels
[e] Calculated using Eqs. (5) and the $g_\parallel$ and $g_\perp$ values listed in Table I.
[f] The special problems associated with the analysis of the experimental results for the $MgO:Cu^{2+}$ system are discussed in detail in Ref. 23.
[g] This represents an approximate value since the value of V_2 obtained in Ref. 2 and for Cu^{2+} in CaO has been employed in Eq. (3).

tems, we find that the q values range from 0.53 to 0.62, with most of the values lying close to 0.56 or 0.57, i.e., the q values are, in every case, significantly larger than 0.5. Accordingly, Eqs. (10) are not adequate for a realistic determination of q in this manner and, therefore, first-order crystal-field theory is not sufficiently precise. For a d^9-configuration ion, the second-order expressions for g_1 and g_2 may be written[38]

$$g_1 = 2.0023 + 4k\lambda/\Delta - (4+k)\lambda^2/\Delta^2 ,$$
$$g_2 = 4k\lambda/\Delta + (2-4k)\lambda^2/\Delta^2 , \qquad (11)$$

where k is a parameter which can be used to make corrections arising from the effects of covalency (i.e., $k=1$ in the absence of covalency and is less than one when covalent effects are significant). Using Eqs. (11), it is then possible to obtain the following expression which relates g_1 and g_2:

$$g_2 = g_1 - 2.0023 + (6-3k)(\lambda^2/\Delta^2) . \qquad (12)$$

If we neglect any possible effects due to covalency (i.e., $k=1$) and use Eq. (12) and the values of qg_2 listed in Table III, we can compute the value of λ/Δ which would be required in order for q to equal 0.5. The values of $\lambda/\Delta = 0.075$, 0.074, and 0.071 are obtained for Ag^{2+} in SrO, CaO, and MgO, respectively. The magnitudes of these values are quite reasonable and, additionally, the variation of the values is completely consistent with the known variation of the strength of the crystalline electric field in these materials (i.e., the crystal field is weakest in SrO and Δ should be smaller than the Δ found for Ag^{2+} in MgO).

The procedure described above is useful in that it indicates that the observed g values are consistent with a value of q close to 0.5 when second-order equations are used with the assumption of reasonable values for λ/Δ. Obviously the reverse procedure would represent the preferred approach [i.e., the experimentally determined values for Δ and λ should be used in Eqs. (11) in order to compute the actual value of q]. The values of Δ for Ag^{2+} in MgO, SrO, and CaO are unfortunately not presently available, however. The effects arising from covalency can of course be quite significant and should be included by means of the appropriate value of k in Eqs. (11). This value of k would, in principal, have to be determined by some independent means. In any event, in view of the uncertainties involved in the determination of q from measured g values, the physical significance of the q values thus determined should not be overemphasized.

The values of A_1 and qA_2 determined for Ag^{2+} in SrO and CaO by means of Eqs. (5) may be employed in Eqs. (10) in order to compute a value for the contact parameter κ. The resulting values of κ for Ag^{2+} in the three alkaline-earth oxides are shown in Table III. These values indicate an effective increase in κ as the JT coupling becomes stronger, but, again, these results should be viewed with an appropriate degree of caution since Eqs. (10) are first-order results. Additionally, the effect of covalency on hyperfine coupling parameters is well established, and Eqs. (10) do not take such effects into account.

V. SUMMARY

The results presented here clearly illustrate the various spectral features associated with the transition from a dynamic to a static Jahn-Teller effect at low temperature. The ability to calculate, in detail, the unusual line shapes and angular variations exhibited by the intermediate JT effect systems serves to firmly establish the applicability of the three-state model to the interpretation of EPR spectra for those systems in which the vibronic singlets are adequately split as a result of the warping terms in the vibronic Hamiltonian. Additionally, a technique has been presented by which it is possible to independently determine the tunneling splitting and the random strain splitting in those cases where the intermediate JT effect is manifested by a lineshape change at the orientation $\vec{H}\|\langle 111\rangle$. This result, in particular, represents a promising technique for the investigation of random strains on a microscopic basis. Additionally, many of the features associated with the transition to an isotropic "averaged" spectrum at elevated temperatures have been illustrated for the three systems investigated here.

ACKNOWLEDGMENTS

The authors are indebted to F. S. Ham for his continuing encouragement and his comments. The excellent technical assistance of E. G. Clardy in many phases of this work is gratefully acknowledged. The authors are particularly indebted to K. A. Müller and W. Berlinger for permission to quote their unpublished results on the averaging observed for Ag^{2+} in CaO powders.

APPENDIX

The details of the calculation used to determine the eigenvalues of the strain, tunneling, Zeeman, and hyperfine interactions operating within the $\psi_{g\theta}, \psi_{g\epsilon}, \psi_{A_2}$ vibronic manifold are presented in this section. The method was successfully applied to the determination of the $CaO:Ag^{2+}$ line shapes at 23 GHz for $\vec{H}\|\langle 111\rangle$.

For the manifold of states consisting of the $\psi_{g\theta}$ and $\psi_{g\epsilon}$ components of the vibronic ^2E state and the A_2 vibronic singlet, the generalized matrix for perturbations within the manifold may be written[1,21,23]

$$\begin{array}{c} \\ \Psi_{A_2}: \\ \Psi_{g\theta}: \\ \Phi_{g\epsilon}: \end{array} \begin{array}{c} \begin{array}{ccc} \Psi_{A_2} & \Psi_{g\theta} & \Psi_{g\epsilon} \end{array} \\ \begin{bmatrix} 3\Gamma + G_1 & rG_\epsilon & -rG_\theta \\ rG_\epsilon & G_1 - qG_\theta & qG_\epsilon \\ -rG_\theta & qG_\epsilon & G_1 + qG_\theta \end{bmatrix} \end{array}, \tag{A1}$$

where G_1, G_θ and G_ϵ are generalized operators having the transformation properties indicated by their respective subscripts and q and r are the Ham reduction factors.[1] The generalized operators for the strain, Zeeman, and hyperfine interactions are given by[1]

$$\begin{aligned} &G_\epsilon = V_2 e_\epsilon, \quad G_\theta = V_2 e_\theta, \quad \text{strain;} \\ &G_1 = g_1 \mu_B \vec{H}\cdot\vec{S}, \quad G_\epsilon = \tfrac{1}{2}\sqrt{3}\, g_2 \mu_B (H_x S_x - H_y S_y), \\ &G_\theta = \tfrac{1}{2} g_2 \mu_B (3H_z S_z - \vec{H}\cdot\vec{S}), \quad \text{Zeeman;} \\ &G_1 = A_1 \vec{I}\cdot\vec{S}, \quad G_\epsilon = \tfrac{1}{2}\sqrt{3} A_2 (I_x S_x - I_y S_y), \\ &G_\theta = \tfrac{1}{2} A_2 (3I_z S_z - \vec{I}\cdot\vec{S}), \quad \text{hyperfine,} \end{aligned} \tag{A2}$$

where V_2 is the strain coupling coefficient, $e_\theta = \frac{1}{2}(2e_{zz} - e_{xx} - e_{yy})$, $e_\epsilon = \frac{1}{2}\sqrt{3}\,(e_{xx} - e_{yy})$, and μ_B is the Bohr magneton.

In order to simplify the diagonalization of Eq. (A1) for the three interactions given in Eq. (A2), a coordinate transformation is desirable. In this transformation, which is similar to that described in Appendix B of Ref. 16, the applied magnetic field $\vec{H}$ is chosen to be parallel to the z' axis of the new coordinate system (x', y', z'). The x' axis is restricted to the old xy plane and both the z' and y' axes are chosen such that an orthogonal right-handed system is formed. If the direction cosines of the z' axis (and therefore of $\vec{H}$) relative to the old (x, y, z) system are denoted by l, m, and n, then the transformed coordinates (x', y', z') are related to the coordinates (x, y, z) by the following transformation:

$$\begin{bmatrix} x' \\ y' \\ z' \end{bmatrix} = \begin{bmatrix} m/\gamma & -l/\gamma & 0 \\ nl/\gamma & nm/\gamma & -\gamma \\ l & m & n \end{bmatrix} \begin{bmatrix} x \\ y \\ z \end{bmatrix}, \tag{A3}$$

and the inverse relationship is given by

$$\begin{bmatrix} x \\ y \\ z \end{bmatrix} = \begin{bmatrix} m/\gamma & ln/\gamma & l \\ -l/\gamma & mn/\gamma & m \\ 0 & -\gamma & n \end{bmatrix} \begin{bmatrix} x' \\ y' \\ z' \end{bmatrix}, \tag{A4}$$

where $\gamma = (l^2 + m^2)^{1/2}$. Since the applied magnetic field $\vec{H}$ is chosen to be along z', it has components $H_x = lH$, $H_y = mH$, and $H_z = nH$ in the old (x, y, z) coordinate system, where $H = |\vec{H}|$. The components of the spin operator $\vec{S}$ in the (x, y, z) system are transformed by the use of Eq. (A4) and are given as follows:

$$\begin{aligned} S_x &= (m/\gamma) S_{x'} + (ln/\gamma) S_{y'} + l S_{z'}, \\ S_y &= (-l/\gamma) S_{x'} + (mn/\gamma) S_{y'} + m S_{z'}, \\ S_z &= -\gamma S_{y'} + n S_{z'}. \end{aligned} \tag{A5}$$

The transformed Zeeman terms of Eq. (A2) are then determined directly by the use of Eq. (A5) and the components lH, mH, and nH. The resulting

transformed G_1, G_θ, and G_ϵ Zeeman terms are given by the following expressions:

$$\begin{aligned} G_1 &= g_1\mu_B H S_{z'}, \\ G_\theta &= \tfrac{1}{2}g_2\mu_B H[(3n^2-1)S_{z'} + \tfrac{3}{2}n\gamma i(S_{+'} - S_{-'})], \\ G_\epsilon &= \tfrac{1}{2}\sqrt{3}\, g_2\mu_B H\{(l^2-m^2)S_{z'} + (lm/\gamma)(S_{+'} + S_{-'}) - \tfrac{1}{2}[ni(l^2-m^2)/\gamma](S_{+'} - S_{-'})\}, \end{aligned} \tag{A6}$$

where

$$S_{x'} = \tfrac{1}{2}(S_{+'} + S_{-'}), \quad S_{y'} = (S_{+'} - S_{-'})/2i.$$

A transformation of the G_1, G_θ, and G_ϵ hyperfine terms as given by Eq. (A4) with the following results:

$$\begin{aligned} G_1 &= A_1(S'\cdot I'), \\ G_\theta &= \tfrac{1}{2}qA_2[(-\tfrac{3}{4}\gamma^2)(S_{+'}I_{+'} + S_{-'}I_{-'}) + \tfrac{1}{4}(3\gamma^2-2)(S_{-'}I_{+'} + S_{+'}I_{-'}) - (3\gamma n/2i)(S_{+'}I_{z'} - S_{-'}I_{z'} + S_{z'}I_{+'} - S_{z'}I_{-'}) + (3n^2-1)S_{z'}I_{z'}], \\ G_\epsilon &= \tfrac{1}{2}\sqrt{3}\, qA_2\{[(n^2+1)(m^2-l^2)/4\gamma^2](S_{+'}I_{+'} + S_{-'}I_{-'}) - (lmni/\gamma^2)(S_{+'}I_{+'} - S_{-'}I_{-'}) + \tfrac{1}{4}(m^2-l^2)(S_{+'}I_{-'} + S_{-'}I_{+'}) \\ &\quad + (l^2-m^2)S_{z'}I_{z'} + \{lm/\gamma - [n(l^2-m^2)/2\gamma]i\}(S_{+'}I_{z'} + S_{z'}I_{+'}) + \{lm/\gamma + [n(l^2-m^2)/2\gamma]i\}(S_{-'}I_{z'} + S_{z'}I_{-'})\}. \end{aligned} \tag{A7}$$

With the inclusion of the Zeeman terms given by Eq. (A6), the 6×6 matrix resulting from Eq. (A1) now has the 36 elements which are tabulated in Table IV. Similarly, the nonzero matrix elements for the transformed hyperfine terms may be calculated using Eq. (A7) particularized to the orientation $\vec{H}\|\langle 111\rangle$ (i.e., $l=m=n=1/\sqrt{3}$).

The matrix for the strain interaction can be formed using the relations given by

$$G_\theta = V_2 e_\theta = \delta\cos\phi/2q, \quad G_\epsilon = V_2 e_\epsilon = \delta\sin\phi/2q, \tag{A8}$$

where δ is given by Eq. (3) and ϕ is determined by $\tan\phi = e_\epsilon/e_\theta$. The resulting matrix of strain and tunneling is as follows:

$$\begin{array}{c} \\ \psi_{A_2} \\ \psi_{g\theta} \\ \psi_{g\epsilon} \end{array} \begin{array}{c} \begin{array}{ccc} \psi_{A_2} & \psi_{g\theta} & \psi_{g\epsilon} \end{array} \\ \begin{bmatrix} 3\Gamma & (r/2q)\delta\sin\phi & (-r/2q)\delta\cos\phi \\ (r/2q)\delta\sin\phi & -\tfrac{1}{2}\delta\cos\phi & \tfrac{1}{2}\delta\sin\phi \\ (-r/2q)\delta\cos\phi & \tfrac{1}{2}\delta\sin\phi & \tfrac{1}{2}\delta\cos\phi \end{bmatrix} \end{array}. \tag{A9}$$

The complete matrix of strain, tunneling, and Zeeman interactions can now be formed by combining the matrix of Eq. (A9) with the matrix elements listed in Table IV. For the orientation $\vec{H}\|\langle 111\rangle$ and with the condition $r = -\sqrt{2}\, q$, this matrix can be written as follows:

$$\begin{array}{c} \\ \psi_{A_2},+\frac{1}{2} \\ \psi_{g\theta},+\frac{1}{2} \\ \psi_{g\epsilon},+\frac{1}{2} \\ \psi_{A_2},-\frac{1}{2} \\ \psi_{g\theta},-\frac{1}{2} \\ \psi_{g\epsilon},-\frac{1}{2} \end{array} \begin{array}{c} \begin{array}{cccccc} \psi_{A_2},+\frac{1}{2} & \psi_{g\theta},+\frac{1}{2} & \psi_{g\epsilon},+\frac{1}{2} & \psi_{A_2},-\frac{1}{2} & \psi_{g\theta},-\frac{1}{2} & \psi_{g\epsilon},-\frac{1}{2} \end{array} \\ \begin{bmatrix} 3\Gamma+\frac{1}{2}\nu & -\frac{1}{2}\sqrt{2}\,\delta\sin\phi & +\frac{1}{2}\sqrt{2}\,\delta\cos\phi & 0 & +\sqrt{2}\,rg_2\nu/4g_1 & -\sqrt{2}\,irg_2\nu/4g_1 \\ -\frac{1}{2}\sqrt{2}\,\delta\sin\phi & \frac{1}{2}(\nu-\delta\cos\phi) & +\frac{1}{2}\delta\sin\phi & \sqrt{2}\,rg_2\nu/4g_1 & -\sqrt{2}\,iqg_2\nu/4g_1 & +\sqrt{2}\,qg_2\nu/4g_1 \\ +\frac{1}{2}\sqrt{2}\,\delta\cos\phi & +\frac{1}{2}\delta\sin\phi & \frac{1}{2}(\nu+\delta\cos\phi) & -\sqrt{2}\,irg_2\nu/4g_1 & +\sqrt{2}\,qg_2\nu/4g_1 & +\sqrt{2}\,iqg_2\nu/4g_1 \\ 0 & \sqrt{2}\,rg_2\nu/4g_1 & +\sqrt{2}\,irg_2\nu/4g_1 & 3\Gamma-\frac{1}{2}\nu & -\frac{1}{2}\sqrt{2}\,\delta\sin\phi & +\frac{1}{2}\sqrt{2}\,\delta\cos\phi \\ +\sqrt{2}\,rg_2\nu/4g_1 & +\sqrt{2}\,iqg_2\nu/4g_1 & +\sqrt{2}\,qg_2\nu/4g_1 & -\frac{1}{2}\sqrt{2}\,\delta\sin\phi & \frac{1}{2}(-\nu-\delta\cos\phi) & +\frac{1}{2}\delta\sin\phi \\ +\sqrt{2}\,irg_2\nu/4g_1 & +\sqrt{2}\,qg_2\nu/4g_1 & -\sqrt{2}\,iqg_2\nu/4g_1 & +\frac{1}{2}\sqrt{2}\,\delta\cos\phi & +\frac{1}{2}\delta\sin\phi & \frac{1}{2}(-\nu+\delta\cos\phi) \end{bmatrix} \end{array} \tag{A10}$$

where the notation $\nu = g_1\mu_B H$ has been employed. As noted previously, the numerical diagonalization was performed only for the 3×3 blocks in Eq. (A10) which were diagonal in spin. These blocks, of course, differ only by ν along the diagonal. The elements which are off-diagonal in spin could be treated by second-order perturbation theory since they are smaller than the difference

TABLE IV. Transformed elements of the matrix of tunneling and Zeeman interactions.

$$
\begin{aligned}
&\langle \psi_{A_2}, \pm\tfrac{1}{2}|\mathcal{H}|\psi_{A_2}, \pm\tfrac{1}{2}\rangle && = 3\Gamma \pm \tfrac{1}{2} g_1 \mu_B H \\
&\langle \psi_{g\theta}, \pm\tfrac{1}{2}|\mathcal{H}|\psi_{g\theta}, \pm\tfrac{1}{2}\rangle && = \pm\tfrac{1}{2}\mu_B H[g_1 - \tfrac{1}{2} q g_2 (3n^2 - 1)] \\
&\langle \psi_{g\epsilon}, \pm\tfrac{1}{2}|\mathcal{H}|\psi_{g\epsilon}, \pm\tfrac{1}{2}\rangle && = \pm\tfrac{1}{2}\mu_B H[g_1 + \tfrac{1}{2} q g_2 (3n^2 - 1)] \\
&\left.\begin{aligned}\langle \psi_{A_2}, \pm\tfrac{1}{2}|\mathcal{H}|\psi_{g\theta}, \pm\tfrac{1}{2}\rangle \\ \langle \psi_{g\theta}, \pm\tfrac{1}{2}|\mathcal{H}|\psi_{A_2}, \pm\tfrac{1}{2}\rangle\end{aligned}\right\} && = \pm\tfrac{1}{4}\sqrt{3}\, r g_2 \mu_B H (l^2 - m^2) \\
&\left.\begin{aligned}\langle \psi_{A_2}, \pm\tfrac{1}{2}|\mathcal{H}|\psi_{g\epsilon}, \pm\tfrac{1}{2}\rangle \\ \langle \psi_{g\epsilon}, \pm\tfrac{1}{2}|\mathcal{H}|\psi_{A_2}, \pm\tfrac{1}{2}\rangle\end{aligned}\right\} && = \mp\tfrac{1}{4} r g_2 \mu_B H (3n^2 - 1) \\
&\left.\begin{aligned}\langle \psi_{g\theta}, \pm\tfrac{1}{2}|\mathcal{H}|\psi_{g\epsilon}, \pm\tfrac{1}{2}\rangle \\ \langle \psi_{g\epsilon}, \pm\tfrac{1}{2}|\mathcal{H}|\psi_{g\theta}, \pm\tfrac{1}{2}\rangle\end{aligned}\right\} && = \pm\tfrac{1}{4}\sqrt{3}\, q g_2 \mu_B H (l^2 - m^2) \\
&\langle \psi_{A_2}, \pm\tfrac{1}{2}|\mathcal{H}|\psi_{A_2}, \mp\tfrac{1}{2}\rangle && = 0 \\
&\langle \psi_{g\theta}, \pm\tfrac{1}{2}|\mathcal{H}|\psi_{g\theta}, \mp\tfrac{1}{2}\rangle && = \mp\tfrac{3}{4} q g_2 \mu_B H n \gamma i \\
&\langle \psi_{g\epsilon}, \pm\tfrac{1}{2}|\mathcal{H}|\psi_{g\epsilon}, \mp\tfrac{1}{2}\rangle && = \pm\tfrac{3}{4} q g_2 \mu_B H n \gamma i \\
&\left.\begin{aligned}\langle \psi_{A_2}, \pm\tfrac{1}{2}|\mathcal{H}|\psi_{g\theta}, \mp\tfrac{1}{2}\rangle \\ \langle \psi_{g\theta}, \pm\tfrac{1}{2}|\mathcal{H}|\psi_{A_2}, \mp\tfrac{1}{2}\rangle\end{aligned}\right\} && = +\tfrac{1}{2}\sqrt{3}\, r g_2 \mu_B H\{lm/\gamma \mp \tfrac{1}{2}[n(l^2 - m^2)i/\gamma]\} \\
&\left.\begin{aligned}\langle \psi_{A_2}, \pm\tfrac{1}{2}|\mathcal{H}|\psi_{g\epsilon}, \mp\tfrac{1}{2}\rangle \\ \langle \psi_{g\epsilon}, \pm\tfrac{1}{2}|\mathcal{H}|\psi_{A_2}, \mp\tfrac{1}{2}\rangle\end{aligned}\right\} && = \mp\tfrac{3}{4} r g_2 \mu_B H n \gamma i \\
&\left.\begin{aligned}\langle \psi_{g\theta}, \pm\tfrac{1}{2}|\mathcal{H}|\psi_{g\epsilon}, \mp\tfrac{1}{2}\rangle \\ \langle \psi_{g\epsilon}, \pm\tfrac{1}{2}|\mathcal{H}|\psi_{g\theta}, \mp\tfrac{1}{2}\rangle\end{aligned}\right\} && = +\tfrac{1}{2}\sqrt{3}\, q g_2 \mu_B H\{lm/\gamma \mp \tfrac{1}{2}[n(l^2 - m^2)i/\gamma]\}
\end{aligned}
$$

in the diagonal terms by a factor of $\sim g_2/g_1$. If we denote the eigenvectors which result from the diagonalization of the blocks which are diagonal in spin as

$$\Phi_{i\pm} = \sum_{j=1}^{3} a_{ij}\psi_{j\pm}\,, \tag{A11}$$

where $\pm$ indicates $\pm M_s$, and $j = 1, 3$ represents a sum over A_2, $E_{g\theta}$, $E_{g\epsilon}$, then the perturbed eigenvalues $E_{i\pm}$ resulting from the operators H_s which are off-diagonal in spin are given as follows:

$$E'_{i\pm} = E_{i\pm} + \sum_{j} \frac{1}{E_{i\pm} - E_{j\pm}} \left| \sum_{k,l=1}^{3} a^*_{ik} a_{jl} \langle \psi_{k\pm} | H_s | \psi_{l\pm} \rangle \right|^2 . \tag{A12}$$

In order to carry out a proper calculation of the line shapes for the orientation $\vec{H} \| \langle 111 \rangle$ it is necessary, of course, to include the hyperfine interaction which has been appropriately transformed using the general results shown in Eq. (A7). In the present calculation, the hyperfine terms were treated using perturbation theory. If we denote the energy levels resulting from the strain, tunneling, and Zeeman interactions as E'_i [Eq. (A12)], then the associated wave functions can be written

$$\Phi_i = \sum_{j=1} a_{ij} |\psi_j\rangle\,,$$

where the summation over j of ψ_j represents a sum over the wave functions in Eq. (A10), and where for constant i, only three values of a_{ij} are in general $\neq 0$. The first-order correction to the energy eigenvalues arising from the hyperfine interaction can be written

$$E'_{i,M_I} = E'_i + \sum a^*_{ik} a_{il} \langle \psi_{kM_I} | H_{HF} | \psi_{lM_I} \rangle + \sum_{M_{I'} \neq M_I} \left| \sum_{k,l=1}^{3} a^*_{ik} a_{il} \langle \psi_{kM_I} | H_{HF} | \psi_{lM_{I'}} \rangle \right|^2 \Big/ (E'_{i\,M_I} - E'_{iM_{I'}}) . \tag{A13}$$

The second-order term, given by

$$\sum_{j \neq i} \frac{1}{E'_i - E'_j} \sum_{M_{I'}} \left| \sum_{k,l} a^*_{ik} a_{jl} \langle \psi_{kM_I} | H_{HF} | \psi_{lM_{I'}} \rangle \right|^2 , \tag{A14}$$

can be shown to be negligible for the present case of Ag^{2+} in CaO. (The nonzero matrix elements $\langle \psi_{kM_I} | H_{HF} | \psi_{lM_I} \rangle$ and $\langle \psi_{kM_I} | H_{HF} | \psi_{lM_{I'}} \rangle$ are computed using the transformed hyperfine operators as indicated earlier.)

The Zeeman and hyperfine interactions were thus taken into account through the use of Eq. (A13). [For example, the EPR magnetic field values were calculated by equating $g_1 \mu_B H$ to the energy difference between allowed transitions in Eq. (A13).]

*Research supported in part by the ERDA under contract with Union Carbide Corp.

[1]F. S. Ham, in *Electron Paramagnetic Resonance*, edited by S. Geschwind (Plenum, New York, 1972). Table II of this reference summarizes the data for those systems which have a ^2E orbital ground state and which exhibit a static JT effect.

[2]R. Englman, *The Jahn-Teller Effect in Molecules and Crystals* (Wiley, London, 1972); see also M. D. Sturge, in *Solid State Physics*, edited by F. Seitz and D. Turnbull (Academic, New York, 1967), Vol. 20.

[3]U. T. Höchli, Phys. Rev. 162, 262 (1967); see also U. T. Höchli and T. L. Estle, Phys. Rev. Lett. 18, 128 (1967).

[4]R. E. Coffman, J. Chem. Phys. 48, 609 (1968).

[5]R. E. Coffman, D. L. Lyle, and D. R. Mattison, J. Phys. Chem. 72, 1392 (1968).

[6]M. C. M. O'Brien, Proc. R. Soc. A 281, 323 (1964).

[7]I. B. Bersuker, Zh. Eksp. Teor. Fiz. 44, 1239 (1963) [Sov. Phys.-JETP 17, 836 (1963)].

[8]I. B. Bersuker, Zh. Eksp. Teor. Fiz. 43, 1315 (1962) [Sov. Phys.-JETP 16, 933 (1963)].

[9]I. B. Bersuker and B. G. Vekhter, Fiz. Tverd. Tela 5, 2432 (1963) [Sov. Phys.-Solid State 5, 1772 (1964)].

[10]Frank S. Ham, Phys. Rev. 166, 307 (1968).

[11]H. C. Longuet-Higgins, U. Öpik, M. H. L. Pryce, and R. A. Sack, Proc. R. Soc. A 244, 1 (1958).

[12]M. S. Child and H. C. Longuet-Higgins, Philos. Trans. R. Soc. Lond. A 254, 259 (1961).

[13]W. Moffitt and W. Thorsen, Phys. Rev. 108, 1251 (1957).

[14]W. Moffitt and W. Thorsen, Phys. Rev. 106, 1195 (1957).

[15]J. R. Herrington, T. L. Estle, L. A. Boatner, and B. Dischler, Phys. Rev. Lett. 24, 984 (1970).

[16]J. R. Herrington, T. L. Estle, and L. A. Boatner, Phys. Rev. B 3, 2933 (1971).

[17]J. R. Herrington, T. L. Estle, and L. A. Boatner, Phys. Rev. B 5, 2500 (1972).

[18]J. R. Herrington, T. L. Estle, and L. A. Boatner, Phys. Rev. B 7, 3003 (1973).

[19]J. R. Herrington, L. A. Boatner, T. J. Aton, and T. L. Estle, Phys. Rev. B 10, 833 (1974).

[20]L. L. Chase, Phys. Rev. Lett. 23, 275 (1969).

[21]L. L. Chase, Phys. Rev. B 2, 2308 (1970).

[22]L. A. Boatner, R. W. Reynolds, M. M. Abraham, and Y. Chen, Phys. Rev. Lett. 31, 7 (1973).

[23]R. W. Reynolds, L. A. Boatner, M. M. Abraham, and Y. Chen, Phys. Rev. B 10, 3802 (1974).

[24]R. W. Reynolds and L. A. Boatner, Phys. Rev. B 12, 4735 (1975).

[25]L. A. Boatner, R. W. Reynolds, M. M. Abraham, and Y. Chen, Bull. Am. Phys. Soc. 18, 448 (1973).

[26]R. W. Reynolds, L. A. Boatner, M. M. Abraham, and Y. Chen, Bull. Am. Phys. Soc. 19, 326 (1974).

[27]L. A. Boatner and R. W. Reynolds, Bull. Am. Phys. Soc. 19, 326 (1974).

[28]S. Guha and L. L. Chase, Phys. Rev. B 12, 1658 (1975); see also S. Guha and L. L. Chase, Phys. Rev. Lett. 32, 869 (1974).

[29]The effective hyperfine parameters A_1 and qA_2 are not to be confused with the A_1 and A_2 which are used to label the irreducible representations of O_h.

[30]M. M. Abraham, C. T. Butler, and Y. Chen, J. Chem. Phys. 55, 3752 (1971).

[31]C. J. Delbecq, W. Hayes, M. C. M. O'Brien, and P. H. Yuster, Proc. R. Soc. A 271, 243 (1963); see also Ref. 32.

[32]J. Sierro, J. Phys. Chem. Solids 28, 417 (1967).

[33]P. Wysling, K. A. Müller, and U. Höchli, Helv. Phys. Acta 38, 358 (1965).

[34]K. A. Müller and W. Berlinger (private communication).

[35]A. M. Stoneham, Proc. Phys. Soc. Lond. 89, 909 (1966).

[36]A. M. Stoneham, Rev. Mod. Phys. 41, 82 (1969).

[37]F. I. B. Williams, D. C. Krupka, and D. P. Breen, Phys. Rev. 179, 225 (1969).

[38]J. R. Herrington, I and B. Dischler (private communication). With g_1 and g_2 written in this form, the following sign convention is applicable: For a d^1-configuration ion in eightfold coordination, replace Δ by $-\Delta$; for a d^9-configuration ion in sixfold coordination, replace Δ by $-\Delta$ and λ by $-\lambda$; for the first-excited state of a d^9-configuration ion in eightfold coordination (i.e., the excited ^2E level), replace λ by $-\lambda$.